# Microphysical Properties of Generating Cells Over the Southern Ocean: Results From SOCRATES

Yang Wang[1,2] (iD), Greg M. McFarquhar[2,3] (iD), Robert M. Rauber[4] (iD), Chuanfeng Zhao[1] (iD), Wei Wu[2] (iD), Joseph A. Finlon[4] (iD), Daniel M. Stechman[2] (iD), Jeffery Stith[5] (iD), Jorgen B. Jensen[5] (iD), Martin Schnaiter[6] (iD), Emma Järvinen[5] (iD), Fritz Waitz[6], Jothiram Vivekanandan[5], Michael Dixon[5] (iD), Bryan Rainwater[7], and Darin W. Toohey[7]

[1]College of Global Change and Earth System Science, State Key Laboratory of Earth Surface Processes and Resource Ecology, Beijing Normal University, Beijing, China, [2]Cooperative Institute for Mesoscale Meteorological Studies, University of Oklahoma, Norman, OK, USA, [3]School of Meteorology, University of Oklahoma, Norman, OK, USA, [4]Department of Atmospheric Sciences, University of Illinois at Urbana-Champaign, Urbana, IL, USA, [5]National Center for Atmospheric Research, Boulder, CO, USA, [6]Karlsruhe Institute of Technology, Institute of Meteorology and Climate Research, Eggenstein-Leopoldshafen, Germany, [7]Department of Atmospheric and Oceanic Sciences, University of Colorado, Boulder, CO, USA

**Abstract** The bulk microphysical properties and number distribution functions ($N(D)$) of supercooled liquid water (SLW) and ice inside and between ubiquitous generating cells (GCs) observed over the Southern Ocean (SO) during the Southern Ocean Clouds Radiation Aerosol Transport Experimental Study (SOCRATES) measured by in situ cloud probes onboard the NCAR/NSF G-V aircraft are compared. SLW was detected inside all GCs with an average liquid water content of $0.31 \pm 0.19 \, \mathrm{g \, m^{-3}}$, 11% larger than values between GCs. The $N(D)$ of droplets (maximum dimension $D < 50 \, \mu m$) inside and between GCs had only slight differences. For ice particles, on the other hand, the mean concentration (median mass diameter) with $D > 200 \, \mu m$ inside GCs was $2.0 \pm 3.3 \, \mathrm{L^{-1}}$ ($323 \pm 263 \, \mu m$), 65% (37%) larger than values outside GCs. As $D$ increases, the percentage differences became larger (up to ~500%). The more and larger ice particles inside GCs suggest the GC updrafts provide a favorable environment for particle growth by deposition and riming and that mixing processes are less efficient at redistributing larger particles. The horizontal scale of observed GCs ranged from 200 to 600 m with a mean of $395 \pm 162 \, m$, smaller than GC widths observed in previous studies. This study expands knowledge of the microphysical properties and processes acting in GCs over a wider range of conditions than previously available.

## 1. Introduction

The term "generating cell" (hereafter GC) describes a small region of locally high radar reflectivity near cloud top, which produces an enhanced reflectivity trail, or fall streak that is characteristic of falling hydrometeors (American Meteorological Society, 2013). Marshall (1953) first introduced the term "generating level" to describe these cells. Subsequent observations noted kilometer-scale GCs atop clouds using vertically upward pointing radars (e.g., Douglas et al., 1957; Gunn et al., 1954; Wexler, 1955). Langleben (1956) used an incoherent scanning radar to deduce that these convective GCs had a lifetime of several hours and were about 1–3 km in horizontal scale and 1 km deep. Thereafter, Heymsfield (1975a) and Carbone and Bohne (1975) applied Doppler radar to estimate vertical velocities of $\pm 1.5 \, \mathrm{m \, s^{-1}}$ and to show the reflectivity maxima were located in the updraft core. More recently, Rosenow et al. (2014) used Doppler radar to show that GCs at the top of the comma head of three continental cyclones were typically 1–2 km deep, about 0.5–2 km in horizontal scale, and had vertical velocities of $\pm 1$–$2 \, \mathrm{m \, s^{-1}}$ (see also Rauber et al., 2015).

In addition to characterizing the properties of GCs, studies have examined the dynamic and thermodynamic processes controlling their development and maintenance. Marshall (1953) showed that GCs provide a favorable environment for the growth of ice crystals subsequently leading to trails of precipitation. Wexler (1955) concluded that ice crystals generated within the tops of cumuliform clouds grow by deposition and riming as they fall. Later, Douglas et al. (1957) observed GCs forming in a stable cloud layer and indicated that latent heat release from deposition was responsible for the observed convection. On the other hand, Wexler and Atlas (1959) suggested that the advection of dry air aloft could lead to convective

instability in a thin generating level and that the growth of ice crystals occurred as they rose and fell within the GCs.

Many of the findings from these ground-based studies have been reassessed from subsequent airborne studies (e.g., Evans et al., 2005; Herzegh & Hobbs, 1980; Heymsfield, 1975b; Hobbs & Locatelli, 1978; Houze et al., 1981; Ikeda et al., 2007; Wolde & Vali, 2002). Aircraft observations over the Northern Hemisphere have shown supercooled liquid water droplets (e.g., Crosier et al., 2014; Field et al., 2004; Ikeda et al., 2007; McFarquhar et al., 2007; Plummer et al., 2014; Rosenow et al., 2014), often occur in the presence of generating cells, indicating updrafts are sufficiently strong to maintain supercooled water even in the presence of significant ice water contents (Kumjian et al., 2014; Rauber & Tokay, 1991). For example, Plummer et al. (2014) showed that updrafts within GCs promote ice nucleation and ice growth using data collected during the 2009–2010 Profiling of Winter Storms (PLOWS) project (Rauber, Wegman, et al., 2014). In addition, they found that GCs are critical for nucleation and initial ice growth even though the growth to larger-size particles took place below the generating-cell level, where enhanced moisture associated with synoptic-scale ascent was present (Plummer et al., 2015). The observation of fall streaks of precipitation emanating from GCs is consistent with the seeder-feeder model of precipitation growth (Bergeron, 1950). Other studies (e.g., Browning, 1983; Cunningham & Yuter, 2014; Herzegh & Hobbs, 1980; Matejka et al., 1980; Rutledge & Hobbs, 1983; Schultz et al., 2004; Trapp et al., 2001) have also interpreted GCs as a seeder-feeder process, with the seeder being the ice particles falling from the cloud-top GCs and the feeder being the supercooled liquid lower within the cloud layer.

Modeling studies have clarified the processes responsible for the growth of precipitation from GCs and for determining environmental conditions under which the GCs can be maintained (Heymsfield, 1975c). For example, Keeler et al. (2016a, 2016b, 2017) used idealized Weather Research and Forecasting (WRF) model simulations initialized with PLOWS observations to show that radiative forcing is critical to GC maintenance under the thermodynamic and vertical wind shear conditions present in winter cyclones (see also Kumjian et al., 2014; Rauber, Macomber, et al., 2014; Rauber, Wegman, et al., 2014).

While most studies describing GCs have focused on continental regions in the Northern Hemisphere, GCs are found elsewhere. For example, McFarquhar et al. (2011) showed that GCs in the Arctic mixed supercooled water throughout cloud due to the inherent turbulence. Although retrievals of large amounts of supercooled water in clouds over the Southern Ocean (SO) have been noted (Hu et al., 2009; Haynes et al., 2011; Huang et al., 2012, 2015), observations of GCs over the SO are scarce due to the lack of in situ and high-resolution remote sensing data. Thus, processes contributing to the formation and dissipation of liquid water and ice particles over the SO are not well understood, and consequently, clouds over the SO are poorly represented in global climate models and reanalysis products (Naud et al., 2014; Trenberth & Fasullo, 2010). To acquire an improved process-based understanding of what controls the amount of supercooled liquid water (SLW) and ice in SO clouds, it is important to characterize the microphysical properties of generating cells over the SO and to compare these properties against those from other regions.

In this study a first characterization of prevalent generating cells observed at the tops of clouds (most are low-level stratus and stratocumulus clouds) over the SO during the Southern Ocean Clouds Radiation Aerosol Transport Experimental Study (SOCRATES) is presented. SOCRATES was conducted between 3 January and 26 February 2018 between Hobart, Australia to 61°S, in the region between 134 °E and 163 °E. This expands the knowledge of the physical properties and processes acting within GCs over a wider range of conditions than previously available. The data acquired during SOCRATES and how they were processed are described in section 2. The structure and microphysical properties of two cases of GCs observed during SOCRATES, one above the boundary layer and another within the boundary layer, are discussed in section 3. A statistical analysis of the microphysical properties observed within and outside of GCs for 15 research flights is presented in section 4. The significance of the findings and principle conclusions are summarized in section 5.

## 2. Data and Methods

The data used in this study were collected during SOCRATES using instruments installed on the National Science Foundation (NSF)/National Center for Atmospheric Research (NCAR) Gulfstream V (G-V)

**Table 1**
*SOCRATES Flight Legs Contained in the Generating Cell Data Set Used in This Study*

| Case no. | Date (UTC) | Time period (UTC) | Length (second) | Avg. alt (km) | Avg. temp (°C) | Avg. lat/lon (°) | Presence of SLW/drizzle |
|---|---|---|---|---|---|---|---|
| 1 | 24 January 2018 | 010650–010810 | 81 | 5.63 | −32.86 | −54.4/141.9 | 1/0 |
| 2 | 24 January 2018 | 010950–011215 | 145 | 5.63 | −32.83 | −54.8/141.6 | 1/0 |
| 3 | 26 January 2018 | 023500–024040 | 341 | 0.77 | −1.82 | −56.2/140.0 | 1/1 |
| 4 | 26 January 2018 | 024200–024330 | 91 | 0.92 | −2.76 | −55.8/139.9 | 1/1 |
| 5 | 29 January 2018 | 014700–015155 | 296 | 0.96 | −7.45 | −61.4/141.2 | 1/1 |
| 6 | 31 January 2018 | 042050–042400 | 191 | 1.52 | −9.66 | −57.4/162.2 | 1/1 |
| 7 | 31 January 2018 | 045800–050000 | 121 | 1.47 | −8.10 | −55.4/160.0 | 1/1 |
| 8 | 04 February 2018 | 030430–030700 | 151 | 1.29 | −10.65 | −61.5/147.0 | 1/1 |
| 9 | 05 February 2018 | 030000–030203 | 125 | 2.17 | −18.81 | −60.7/158.8 | 1/0 |
| 10 | 07 February 2018 | 214220–214510 | 171 | 7.25 | −28.35 | −47.8/146.2 | 1/0 |
| 11 | 08 February 2018 | 003000–003400 | 241 | 2.38 | −15.00 | −61.4/145.1 | 1/1 |
| 12 | 08 February 2018 | 013800–014040 | 161 | 1.03 | −2.61 | −56.6/146.0 | 1/1 |
| 13 | 08 February 2018 | 022440–022920 | 281 | 1.20 | −2.72 | −53.2/146.4 | 1/1 |
| 14 | 18 February 2018 | 033500–033800 | 181 | 0.95 | −6.24 | −59.4/141.5 | 1/1 |
| 15 | 18 February 2018 | 042750–043000 | 131 | 1.20 | −6.63 | −56.0/141.5 | 1/1 |
| 16 | 20 February 2018 | 021900–022400 | 301 | 0.95 | −1.93 | −53.4/157.5 | 1/1 |

*Note.* The number "1" represents the presence of supercooled liquid water (SLW) and/or drizzle for each time period based on the RICE measurements for temperatures lower than −4°C, and the 2DS/2DC/PHIPS phase information if the temperature was higher than −4°C. The presence of drizzle was identified by the PHIPS when liquid particles with $D > 100$ μm were present.

aircraft, also known as the High-Performance Instrumented Airborne Platform for Environmental Research (HIAPER). Instruments included an aircraft cloud radar (the HIAPER Cloud Radar, HCR), a High Spectral Resolution Lidar (HSRL), and a suite of in situ microphysical probes. All data used were collected during 15 research flights, which took place between 15 January and 24 February 2018.

### 2.1. Instruments

The HCR is an airborne, dual-polarization, W-band Doppler radar that detects drizzle (refer to liquid drops with maximum dimension larger than 100 microns), ice, and cloud droplets. It provides measurements of Doppler radial velocity (W) and equivalent radar reflectivity factor ($Z_e$) (Vivekanandan et al., 2015). The HCR was typically rotated to point upwards when flying beneath or ascending through boundary layer clouds and downwards at other times. In this study, $Z_e$ and W had a range resolution of about 18 m (unambiguous range of 15 km) and along-flight track resolution of 60 m. Sixteen cases when GCs were observed near cloud top are summarized in Table 1. Because the HCR has a dead zone of 145 m where data are not useable, measurements of $Z_e$ and W at the location of the G-V are not available. Therefore, it was assumed that the first useable HCR gate (i.e., eight range gate) beneath the G-V gave $Z_e$ and W corresponding to the cloud properties derived from the in situ probes at flight altitude (given as altitude above mean sea level, hereafter). Note that the radial velocity was carefully corrected for platform motion using two different methods. The first corrects for platform motion using INS/GPS measurements, which was applied for all data. An additional correction was applied to the nadir-looking data only: The radial velocity of the surface, which is assumed to be 0 m s$^{-1}$, is used as a reference to correct the data following Ellis et al. (2017).

Measurements are also available from the HSRL, an eye-safe calibrated lidar system that measures backscatter coefficient and depolarization properties of atmospheric aerosols and clouds and retrieves cloud extinction coefficient with a temporal resolution and range resolution of 0.5 s and 7.5 m, respectively (UCAR/NCAR-Earth Observing Laboratory, 2018). In this study, the particle depolarization ratio ($\delta_p$) from the HSRL was used to identify the vertical distributions of SLW.

In addition, the presence of SLW was identified using a Rosemount Icing Detector (RICE). A voltage change of at least 2 mV s$^{-1}$ at temperatures less than −4°C indicates the existence of SLW (Cober et al., 2001). The RICE does not detect the presence of SLW at higher temperatures (>−4°C) due to the dynamic heating of the probe (Cober et al., 2001; McFarquhar et al., 2007).

The number distribution functions for cloud particles were measured by a Cloud Droplet Probe (CDP) for particles with maximum dimensions $D$ between 2 and 50 μm, a 10 μm resolution 2D-Stereo probe (2DS)
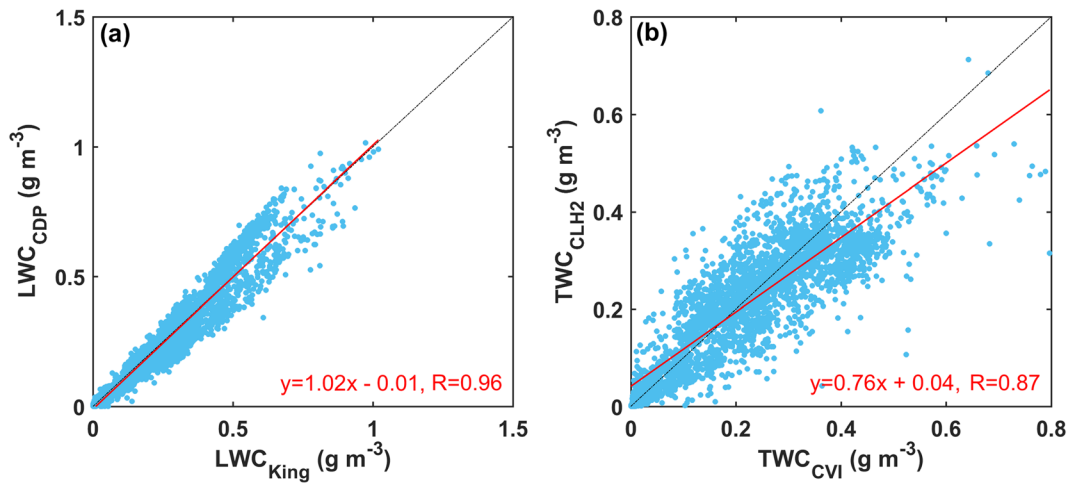
**Figure 1.** (a) King probe LWC (LWC$_{King}$) versus LWC derived from the CDP SDs (LWC$_{CDP}$) and (b) TWC measured from CVI probe (TWC$_{CVI}$) against that measured from CLH2 probe (TWC$_{CLH2}$). All cases referenced in Table 1 are included. The red line is the linear best fit line, and the red text shows the best linear fit equation and correlation coefficient (R).

nominally sizing particles with $10 < D < 1280$ μm, and by a Fast Two-Dimensional Cloud Probe (2DC) nominally sizing particles between 25 and 1,600 μm with 25 μm resolution. The maximum dimension $D$ applied for 2DS/2DC is the diameter of smallest circle enclosing particle (Wu & McFarquhar, 2016). The 2DS and 2DC data were processed using the University of Illinois/Oklahoma Optical Array Probe Processing Software (UIOOPS, McFarquhar et al., 2018). UIOOPS includes corrections for out of focus particles following Korolev (2007), and particles whose center is inside the photodiode array are reconstructed following Heymsfield and Parrish (1978). Shattered artifacts are eliminated by rejecting all particles with inter-arrival times below a time varying threshold (Field et al., 2006). Given the large uncertainties in the probe's depth of field for small particle sizes in the first several bins (Baumgardner & Korolev, 1997), particles with $D < 50$ μm for the 2DS and $D < 150$ μm for the 2DC were not included in the analysis. Numerous morphological properties were calculated for individual particles such as the particle maximum dimension, projected area, and perimeter, with particle habit identified following the algorithm by Holroyd (1987). The number distribution function $N(D)$ from the 2DS/2DC was determined for each second of flight. Thereafter, the mass distribution function, $M(D)$, and the ice water content (IWC) from the 2DS/2DC were derived using the projected area of an individual particle following power-law mass-dimensional relationship by Baker and Lawson (2006). The $M(D)$ for drizzle was calculated separately as liquid drops. Considering the small size of the GCs in this study, the one second resolution is needed in order to characterize the microphysical properties of GCs, even though a longer
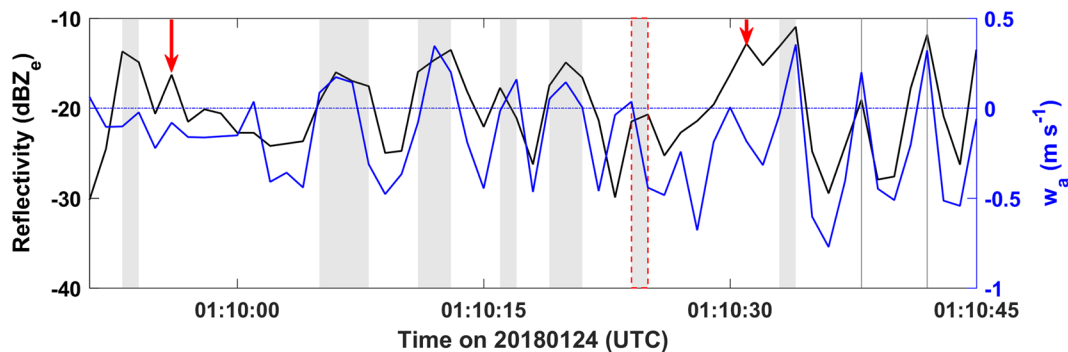


**Figure 2.** Schematic showing approach to define the GC locations. The black line and blue line show Z$_e$ and vertical velocity ($w_a$) as a function of time, respectively. The red arrows show the locations with prominence smaller than 4 dBZ$_e$. Shaded areas show the identified GC locations with red dashed lines indicating the velocity of a peak is smaller than the 25th percentile of the velocity distribution of the cloud leg and hence not identified as a GC.
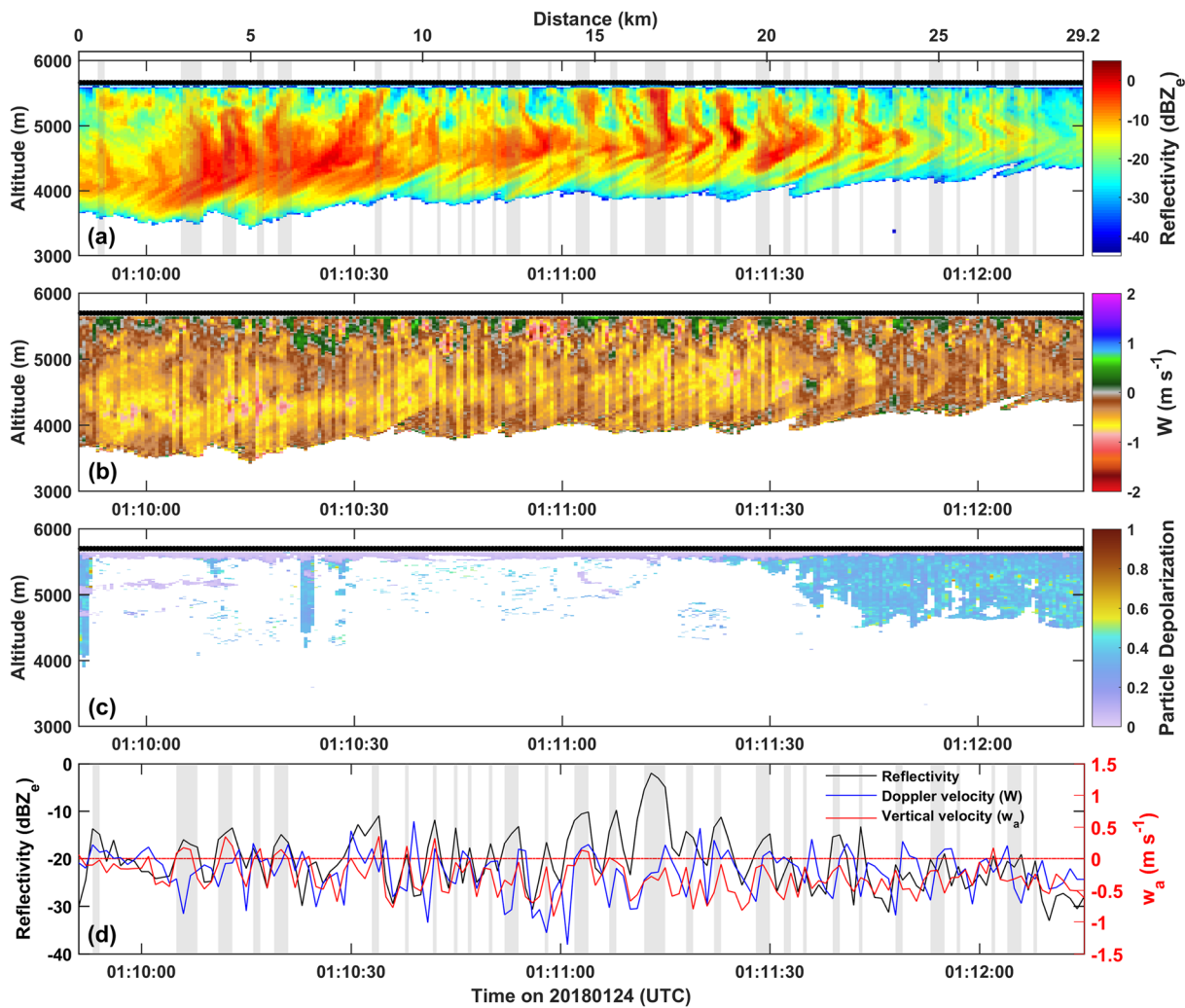
**Figure 3.** Altitude-time cross sections of (a) HCR $Z_e$, (b) HCR Radial velocity, and (c) HSRL particle depolarization. (d) Time series of the eigth range gate reflectivity (black line), Doppler vertical radial velocity (W, blue line), and vertical velocity measured from the aircraft ($w_a$, red line) over the time period between 010930 to 011230 (UTC) 24 January 2018 flight leg of case no.2. The black lines in (a), (b), and (c) show the flight level of the G-V aircraft. The horizontal red dashed line in (d) represents $w_a = 0$ m s$^{-1}$. The shadow regions in both (a) and (d) show the GC locations identified by the method described in section 2.2.

averaging period would be better to get a more statistically significant measure (e.g., McFarquhar et al., 2007).

In this study, SLW was first identified for each second of flight using the RICE detector for temperatures less than −4°C and the 2DS/2DC phase information provided by UIOOPS for temperatures greater than −4°C. Then if the number concentration from the 2DS/2DC with $D > 200$ µm for nonspherical particles (based on particle habit product by UIOOPS described above) is larger than 0 L$^{-1}$, it was assumed to have ice particles. Thus, the cloud phase (liquid-, ice- or mixed-phase) for every second of each of the flight legs shown in Table 1 was determined. Inspections of the 2DS, 2DC, and PHIPS (Particle Habit Imaging and Polar Scattering probe, Abdelmonem et al., 2016, Schnaiter et al., 2018) images were used to confirm the presence of ice particles. The PHIPS single particle measurements were also used to confirm particle microphysical properties as well as to discriminate ice from droplets based on angular light scattering measurements (Schnaiter, 2018; Schnaiter et al., 2018). The presence of drizzle was identified by the PHIPS angular light scattering data when liquid particles with $D > 100$ µm were present.

For mixed-phase clouds, it was assumed that the CDP $N(D)$ represented SLW droplets for $2$ µm $< D < 50$ µm because the small particles ($D < 50$ µm) in mixed-phase clouds are most likely supercooled water (McFarquhar et al., 2007, 2011; McFarquhar & Cober, 2004). During SOCRATES, PHIPS single particle
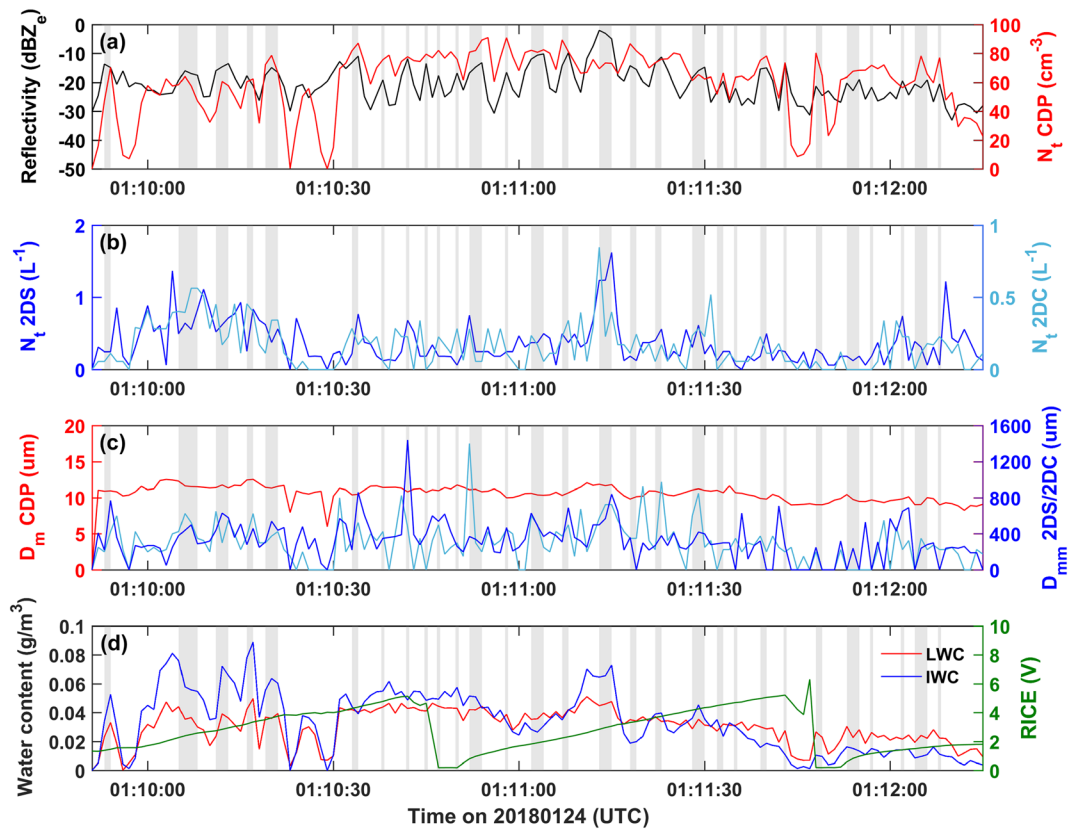
**Figure 4.** Time series of (a) $Z_e$ (black line) and total number concentration ($N_t$) of CDP (red line); (b) 2DS $N_t$ (blue line) and 2DC $N_t$ (light blue line); (c) CDP $D_{mm}$ (red line) and 2DS/2DC $D_{mm}$ (blue/light blue line); and (d) King probe LWC (red line), IWC estimated from 2DS $N(D)$ based on mass-diameter relationships (blue line) and RICE voltage (green line) for the 010950–011215 UTC 24 January 2018 flight leg. The shaded gray boxes represent the identified locations of GCs.

angular scattering data show that 10% (0.6%) of the drops were larger than 150 μm (200 μm) on average for all selected flight legs shown in Table 1. Thus, the nonspherical particles with $D > 2000$ μm from the 2DS were assumed to be ice, and spherical particles with 50 μm $< D <$ 200 μm from 2DS were assumed to be liquid droplets when drizzle was present. If the drizzle was not present, particles with $D > 50$ μm were assumed to be ice following McFarquhar et al. (2007).



**Figure 5.** Selected 2DS images of (a) inside the GCs and (b) outside the GCs for particles with $D > 50$ μm over the time period of case no. 2. Images shown here are for particles accepted by UIOOPS with area ratio > 0.4.

**Table 2**
*The Correlation Coefficient Between Different Variables with $Z_e$ and $w_a$ for Case no. 2 and no. 16*
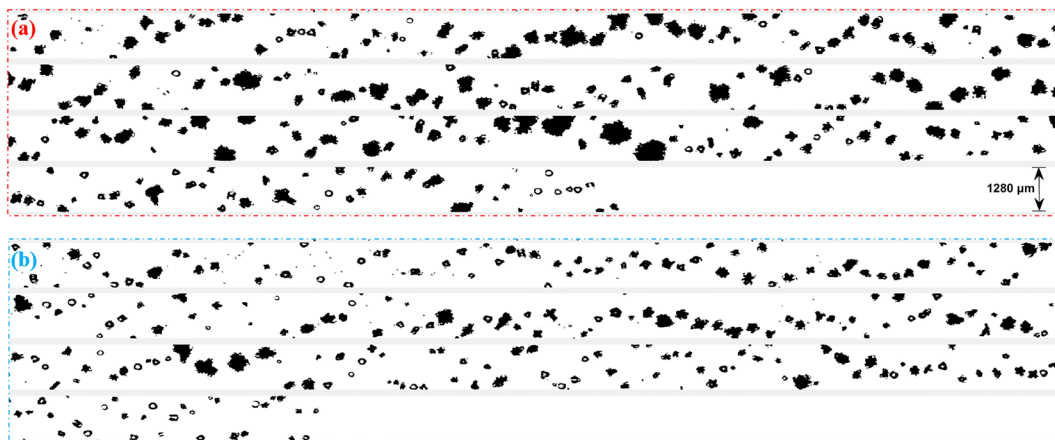
| Case no. 2 | $w_a$ | $N_t$ CDP | $N_t$ 2DS | $N_t$ 2DC | $N_{2DS > 150}$ | $D_m$ CDP | $D_{mm}$ 2DS | $D_{mm}$ 2DC | $D_{mm\ 2DS > 200}$ | LWC | IWC |
|---|---|---|---|---|---|---|---|---|---|---|---|
| $Z_e$ | 0.46 | 0.47 | 0.32 | 0.26 | 0.42 | 0.28 | 0.45 | 0.41 | 0.48 | 0.45 | 0.40 |
| $w_a$ | 1.00 | 0.07 | 0.23 | 0.20 | 0.19 | 0.11 | 0.41 | 0.23 | 0.45 | 0.08 | 0.20 |

| Case no. 16 | $w_a$ | $N_t$ CDP | $N_{50 < 2DS < 200}$ | $N_t$ 2DC | $N_{2DC > 200}$ | $D_m$ CDP | $D_{m\ 50 < 2DS < 200}$ | $D_{mm}$ 2DC | $D_{mm\ 2DC > 200}$ | LWC | IWC |
|---|---|---|---|---|---|---|---|---|---|---|---|
| $Z_e$ | 0.59 | 0.37 | 0.34 | 0.62 | 0.65 | −0.04 | 0.61 | 0.36 | 0.40 | 0.38 | 0.42 |
| $w_a$ | 1.00 | 0.22 | 0.23 | 0.59 | 0.56 | −0.08 | 0.59 | 0.40 | 0.43 | 0.36 | 0.41 |

The bulk liquid water content (LWC) was measured by a Commonwealth Scientific and Industrial Research Organization (CSIRO) King probe (King et al., 1978), which has a 15% uncertainty (King et al., 1985). Past studies (e.g., Cober et al., 2001) have suggested the King probe can also respond by an average of 20% to the presence of IWC. Some studies (e.g., Dorsi, 2013) have accordingly reduced the LWC by some fraction of the bulk water content measured by a cloud condensed water content (TWC) probe. However, for all the cloud top cases listed in Table 1, Figure 1a compares the LWC measured by the King probe with that derived from the CDP droplet size distribution. The LWC$_{King}$ is broadly consistent with that derived by
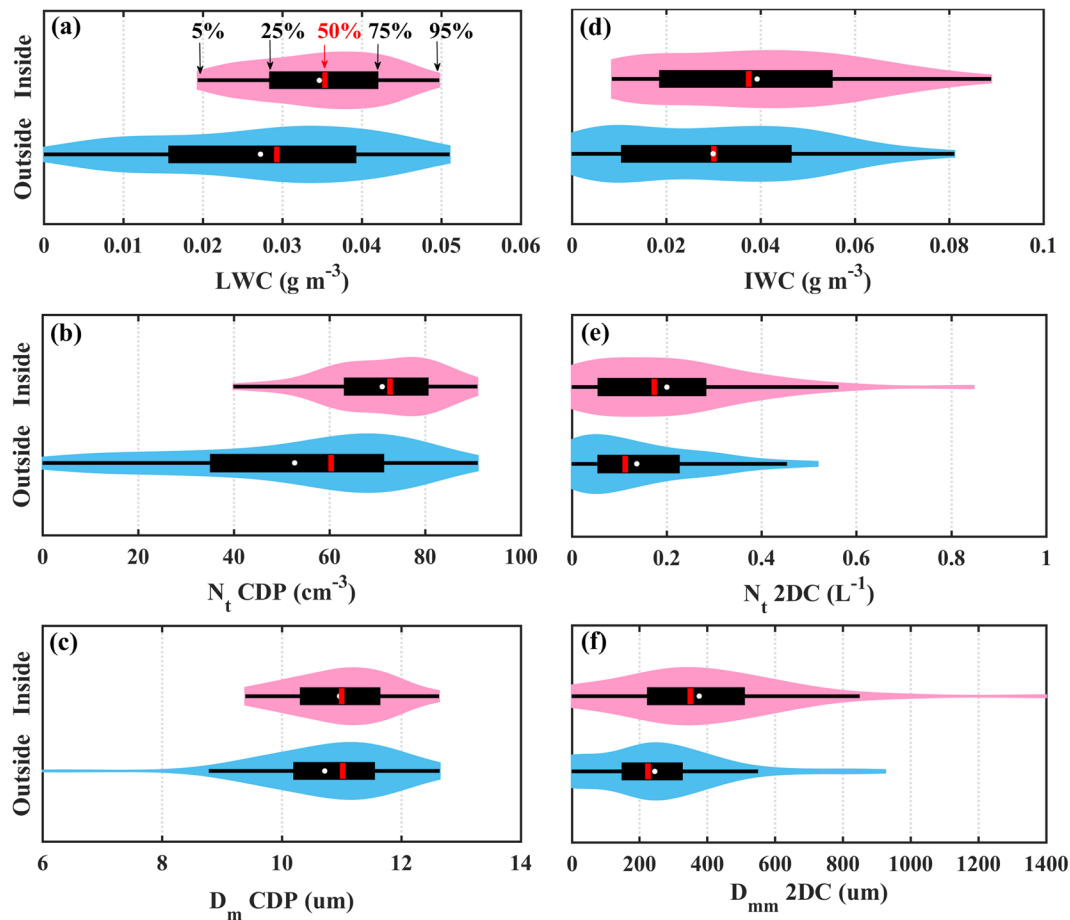


**Figure 6.** Statistical results of case no. 2 shown by Kernel probability density distributions of microphysical properties inside (pink color) and outside GCs (blue color) for (a) LWC, (b) CDP $N_t$, (c) mass mean diameter ($D_m$) of CDP, (d) IWC, (e) 2DC $N_t$, and (f) median mass diameter ($D_{mm}$) of 2DC. The black boxplots, from left to right, show the 5th, 25th, 50th (red line), 75th, and 95th range of the data in each distribution. The white points in the boxplots indicate the mean values. The width of red and blue shaded area represents the the proportion of the data located there.

**Figure 7.** As in Figure 3, but over the time period between 031900 to 032400 (UTC) 20 February 2018 flight leg of case no. 16.

integrating the CDP size distribution, $LWC_{CDP}$. The root mean square error (RMSE) and correlation coefficient (R) are 0.057 g m$^{-3}$ and 0.96, respectively, and the best linear fit is

$$LWC_{CDP} = 1.02 LWC_{King} - 0.01\ g\ m^{-3}. \qquad (1)$$

Therefore, the LWC in this study refers to that measured by the King probe unless otherwise specified.
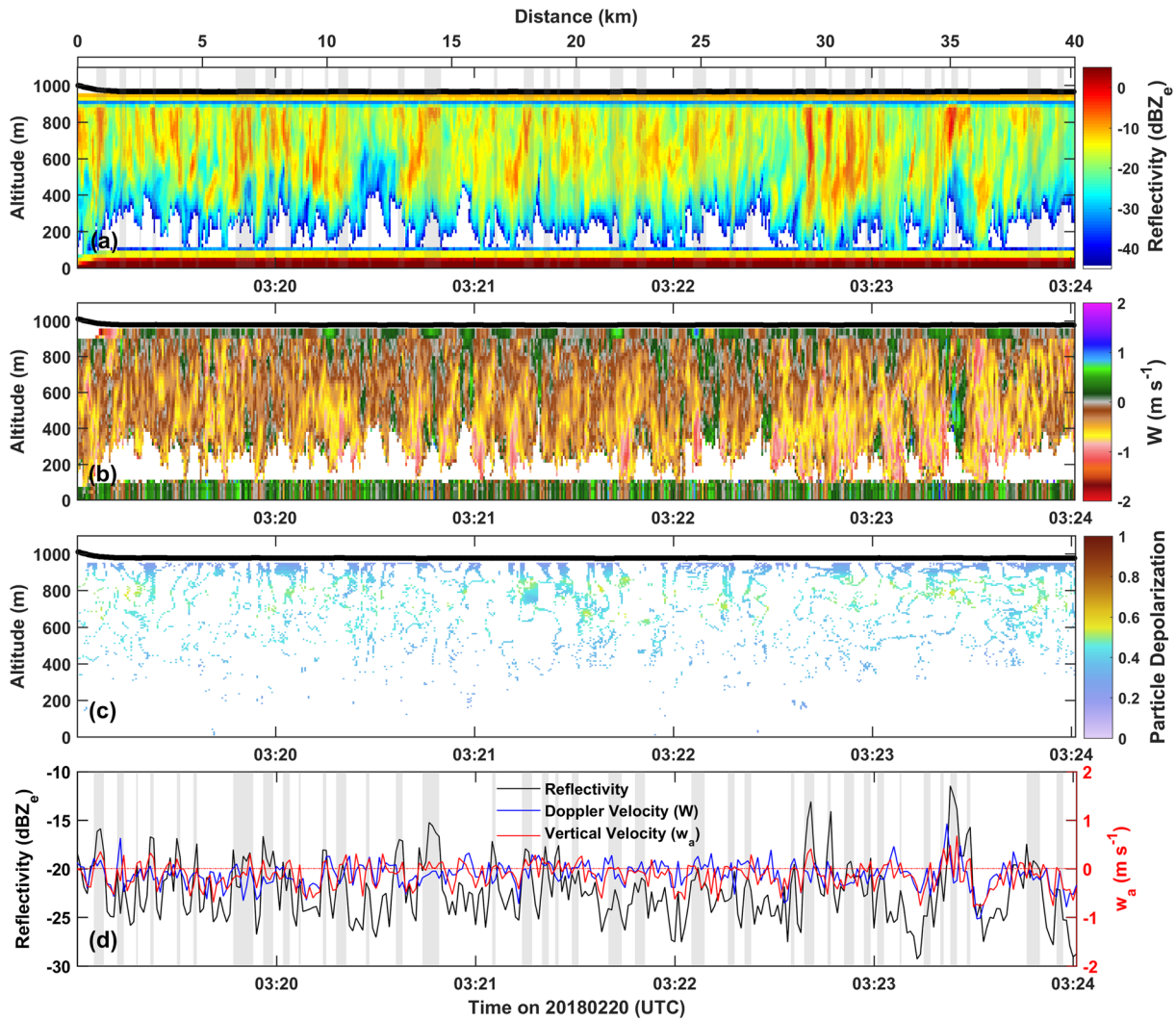
The Counterflow Virtual Impactor (CVI) provides bulk measures of TWC greater than 1 mg m$^{-3}$ by evaporating particles in dry air and measuring the resulting vapor using a tunable diode laser absorption hygrometer (Twohy et al., 2003). The CVI TWC is estimated to have an uncertainty of approximately 15% (Baumgardner et al., 2017). The University of Colorado Closed-Path Hygrometer (CLH-2, Dorsi et al., 2014) provides another measure of bulk TWC by using a laser spectrometer to measure the water vapor resulting from the vaporization of condensed water in a heated inlet. The measurement frequency and horizontal resolution are 1 Hz and 200 m, respectively, at a nominal true airspeed of 200 m s$^{-1}$. The CLH-2 TWCs are corrected for inertial enhancement of particle concentrations and for the calibration of the flow controller due to the accumulation of the small dust/sand grains in the flow-sensing element (Toohey & Rainwater, 2019). The uncertainty is estimated at 20%. Figure 1b shows that the TWC measured from the CVI ($TWC_{CVI}$) agrees with that measured from the CLH-2 ($TWC_{CLH2}$), with the RMSE and R of 0.057 g m$^{-3}$ and 0.87. The best linear fit function is given by
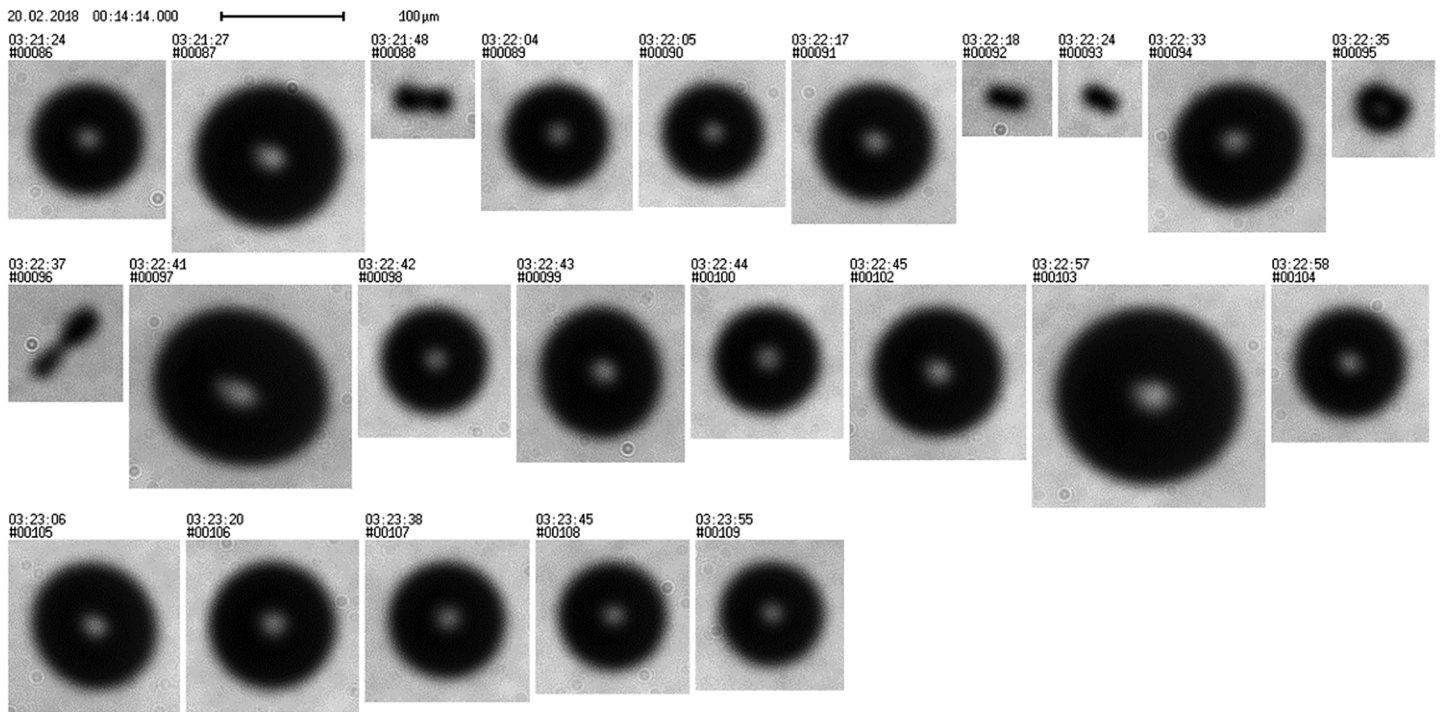
**Figure 8.** The PHIPS images during 032124–032355 UTC 20 February 2018 of case no. 16.

$$TWC_{CLH2} = 0.76 TWC_{CVI} + 0.04 \, g \, m^{-3}. \tag{2}$$

Because the TWC within the mixed-phase clouds measured during SOCRATES was typically dominated by supercooled water, it is not possible to subtract $LWC_{King}$ from TWC to obtain the IWC: This would be a small difference between two larger numbers subject to considerable uncertainty (McFarquhar et al., 2007). Thus, the IWC was obtained by integrating the 2DS ice particle size and projected area distributions following Baker and Lawson (2006). The overall frequency from the 2DC of particles with $D > 1,280 \, \mu m$ for the entire selected data set was ~2%. Therefore, the 2DS $M(D)$ was used only in this study for the IWC calculations.

Except for the 2DS and 2DC processing described above, all other data sets (e.g., the temperature ($T$), vertical velocity ($w_a$) from the gust probe onboard the aircraft, King probe, CDP and RICE data) were processed at the NCAR Research Aviation Facility (RAF) and included in the "Low Rate (1 Hz) Navigation, State
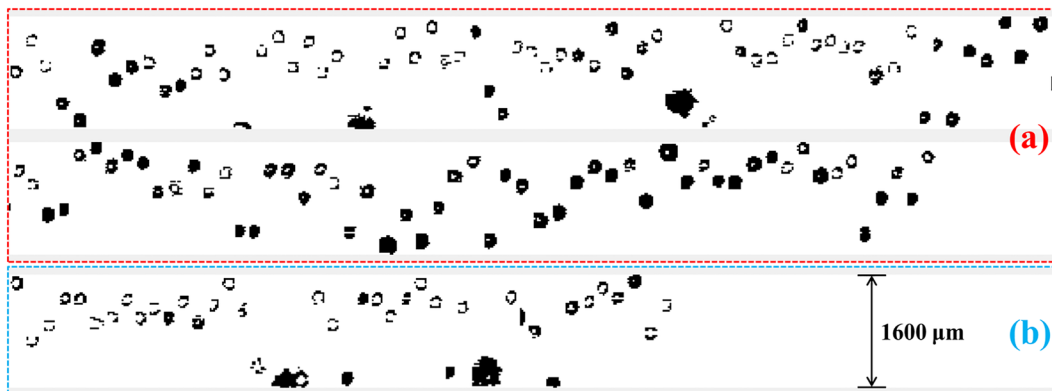


**Figure 9.** Selected 2DC images of (a) inside the GCs and (b) outside the GCs for particles with $D > 200 \, \mu m$ for the time period of case no. 16. Images shown here are particles all accepted by UIOOPS with area ratio > 0.4.
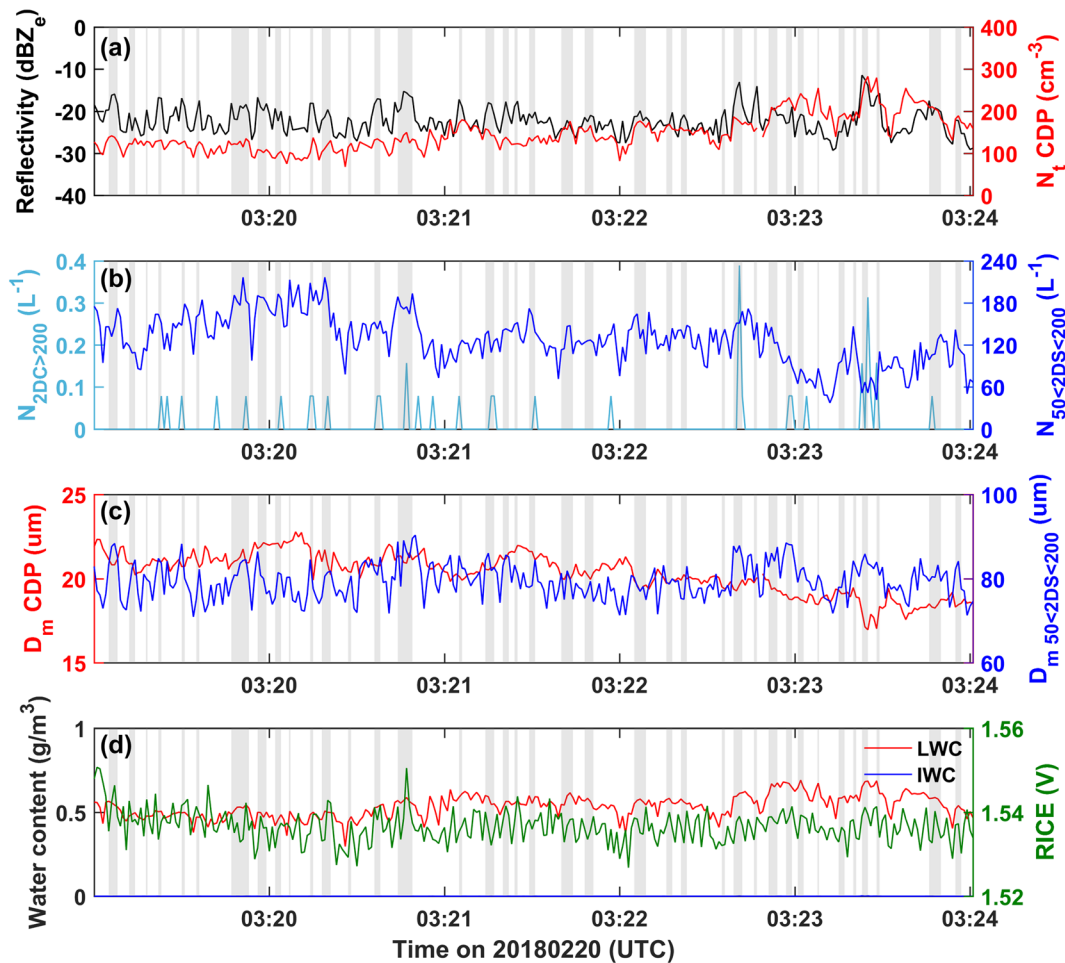
**Figure 10.** (a) and (d) are the same as Figure 4 but for the time period of case no. 16. Note that (b) shows the concentrations of 2DS for particle with $50 < D < 200$ μm ($N_{50 < 2DS < 200}$, blue line) and 2DC for particle with $D > 200$ μm ($N_{2DC > 200}$, light blue line). (c) shows the mass mean diameter $D_m$ from CDP (red line) and the mass mean diameter from 2DS for particles with $50 < D < 200$ μm ($D_{m\ 50 < 2DS < 200}$, blue line).

Parameter, and Microphysics Flight-Level Data" product (UCAR/NCAR-Earth Observing Laboratory, 2018). The 2DS and 2DC data in this product were compared with those processed by UIOOPS for all the selected cases to ensure that the 2DS and 2DC probes were functioning properly and the data quality was good.

### 2.2. Method of Generating Cell Identification

For midlatitude winter cyclones, Plummer et al. (2014) determined the locations of GCs using $Z_e$ measured by the Wyoming Cloud Radar, assuming points within $\pm 2$ s of all 4-dB local maxima in $Z_e$ were within the GCs. To account for the fact that the horizontal scale of GCs is not constant, an alternate method was used to identify the GC locations for SOCRATES using the $Z_e$ measured by the HCR at the closest usable range gate to the aircraft. Figure 2 shows a schematic illustrating the approach to identify GC locations using the HCR $Z_e$ measured for a constant altitude leg flown at a temperature of $-32.8°C$ and an altitude of 5.63 km between 010950 to 011045 UTC on 24 January 2018. Several local maxima corresponding to enhanced reflectivity and rising motion within GCs are indicated by gray shading.

All reflectivity peaks with prominence $\geq 4$ dBZ$_e$ are first identified. The prominence of a peak defines how much the peak stands out due to its intrinsic height and its location relative to other peaks. The specific definition of prominence and algorithm to compute it are found at https://www.mathworks.com/help/signal/ug/prominence.html. A low isolated peak can be more prominent than one peak with larger $Z_e$ that is otherwise unremarkable depending on the $Z_e$ of the surrounding clouds. For example, peaks with prominence <4
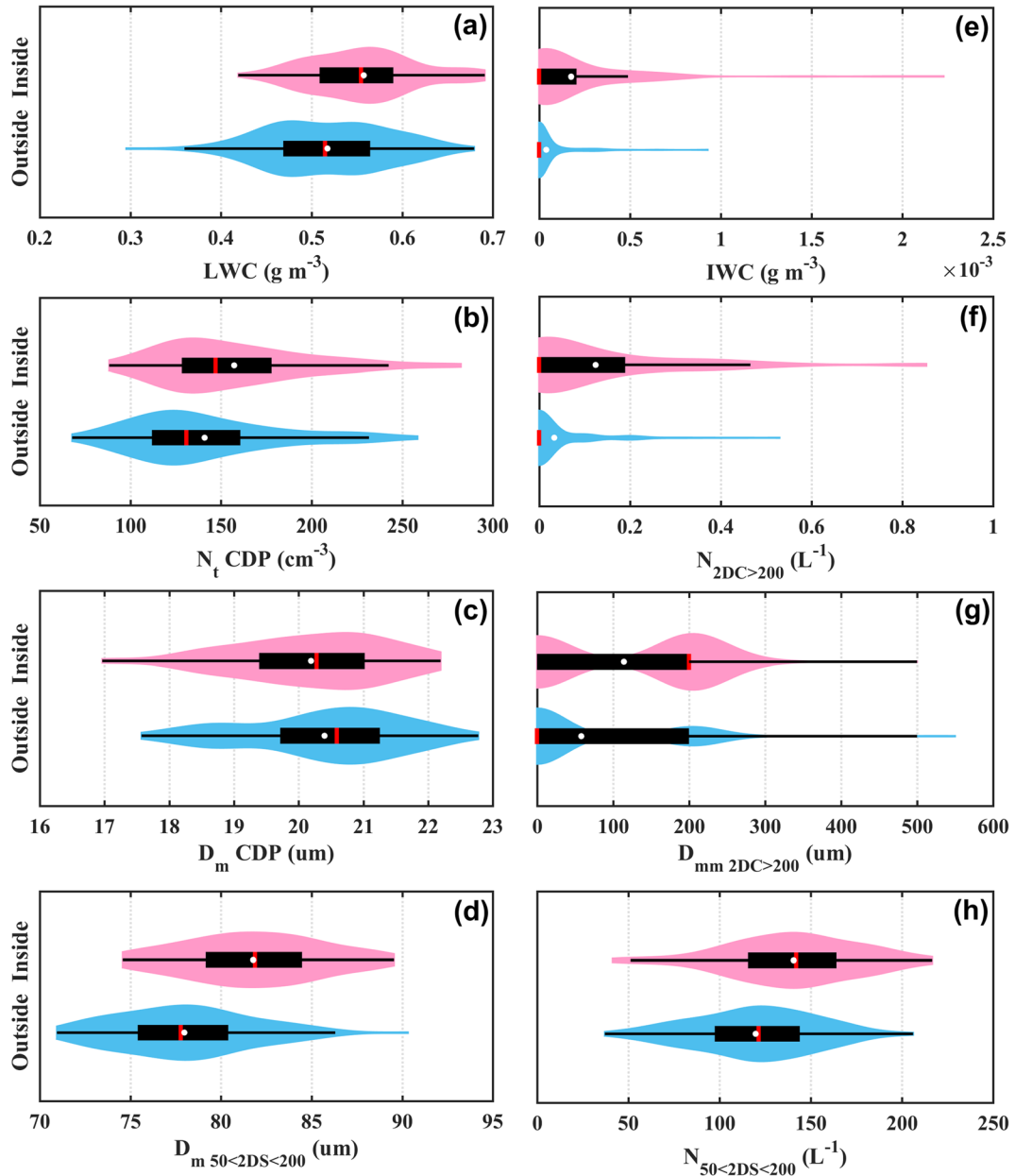
**Figure 11.** Statistical distributions of case no. 16 shown by Kernel probability density distributions of microphysical properties inside (pink color) and outside GCs (blue color) for (a) LWC, (b) CDP $N_t$, (c) mass mean diameter of CDP ($D_m$ CDP), (d) mass mean diameter with 50 μm $< D <$ 200 μm ($D_{m\ 50\ <\ 2DS\ <\ 200}$), (e) IWC, (f) the concentrations of 2DS with $D >$ 200 μm ($N_{2DS\ >\ 200}$), (g) median mass diameter with $D >$ 200 μm ($D_{mm\ 2DS\ >\ 200}$), and (h) number concentration with 50 μm $< D <$ 200 μm ($N_{50\ <\ 2DS\ <\ 200}$) for droplets from 2DS. The black boxplots, from left to right, show the 5th, 25th, 50th (red line), 75th, and 95th range of the data in each distribution. The white points in the boxplots indicate the mean values. The width of dark red and blue shaded areas represents the proportion of the data located there.

dBZ$_e$ shown by the red arrows in Figure 2 are not identified as peaks. Sensitivity analysis using different prominence thresholds to define the location of GCs did not perform as well for identifying the GCs. Therefore, the 4-dBZ$_e$ threshold was used.

After identifying the peaks, times corresponding to Z$_e$ within 4 dBZ$_e$ of the peak value were identified as within the GCs (Figure 2). To avoid identifying small peaks in Z$_e$ that are not accompanied by rising motion, GCs with $w_a$ at peak Z$_e$ less than the 25th percentile of the velocity distribution for the cloud leg were removed. An example of a GC removed by this criterion is shown by the red dashed line in Figure 2.
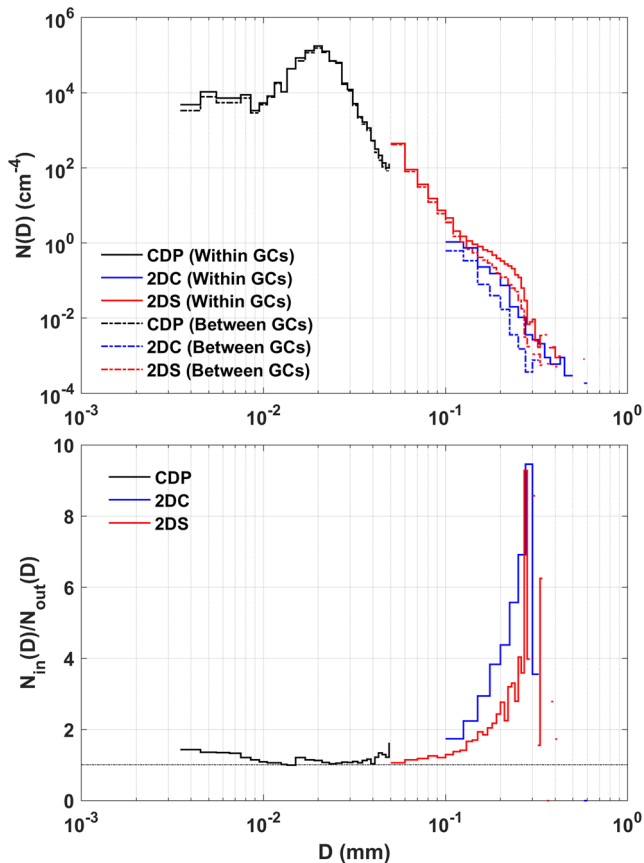
**Figure 12.** (a) Average number distribution functions, $N(D)$, within (solid lines) and between (dashed lines) the GCs. (b) The ratio of the average number distribution functions measured inside GCs, $N_{in}(D)$, to average number distribution functions measured between GCs, $N_{out}(D)$, from CDP (black), 2DC (blue) and 2DS (red) for the entire GC data set. The black dashed line shows the ratio value of 1.

After identifying the GCs for all legs, the microphysical properties within and between the GCs measured by the in situ cloud probes were computed, with distributions inside and outside the GCs contrasted as shown in section 3. The significance of the differences in cloud properties within and between the GCs were tested using a one-way analysis of variance under a confidence level of 0.05.

## 3. Case Studies

During SOCRATES, numerous GCs at cloud top where the cloud top altitude was 1 to 2 km were sampled in the boundary layer (whose top altitude was retrieved by the inversion layer altitude from the G-V temperature profile). In addition, several cases of cloud top GCs well above the boundary layer were measured. In order to illustrate specific characteristics of the small-scale structures within GCs and the role of microphysical processes acting inside and outside GCs, two GC cases observed during SOCRATES are discussed in detail. Thereafter, a statistical analysis of the properties of all GCs observed near cloud top during SOCRATES is presented in section 4. The two specific GCs discussed in this section are those measured in a higher-level cloud with altitude of about 5.6 km on 24 January 2018 and in a boundary layer cloud with cloud top altitude of about 0.9 km on 20 February 2018. The two cases represent typical characteristics of GCs at different altitudes/temperatures.

### 3.1. Generating Cells Within a High-Level Cloud

Figures 3a–3c show altitude-time cross sections of $Z_e$, W, and $\delta_p$ measured by the downward pointing HCR and HSRL between 010930 and 011230 on 24 January 2018. Figure 3d shows the time series of $Z_e$, W (both 145 m below the G-V), and $w_a$. At the time of these observations, the G-V (shown by the black line) was flying near the tops of clouds with a mean temperature of −32.8°C and top altitude of 5.6 km MSL. Figure 3a shows that fall streaks of enhanced reflectivity were present at and below the flight level. The shaded gray areas in Figure 3 correspond to the GC locations identified by the method described in section 2.2, which appears to successfully identify the GC locations. The horizontal scale of the GCs ranges from 1 to 5 s (i.e., 200.2 to 1009.8 m given the true air speed of the G-V) with a mean width of 402 m for this flight leg. This is considerably narrower than the mean GC width of 0.5–2 km for midlatitude winter cyclones quoted by Rosenow et al. (2014). Another observed feature is the fine scale variation of the vertical velocity in Figure 3b near and beneath the flight track. There was a close proximity of updrafts and downdrafts at the flight level near cloud top, resulting in high-frequency vertical stripes, which were also noted by Plummer et al. (2014). In fact, Figures 3b and 3d show the measured W and $w_a$ vary between −1.5 and 1.0 m s$^{-1}$ on a fine scale (~200–400 m), showing that the G-V went through alternating updrafts and downdrafts at flight level. Deeper within the cloud, the Doppler velocities (the sum of the air vertical velocity and the particle fall speed) still exhibit fine-scale variation as seen within the stripes. This is associated with the larger fall speeds (~5 m s$^{-1}$) acquired by larger particles as they grow by deposition, riming, and aggregation within the fall streaks. The vertical distribution of $\delta_p$ in Figure 3c demonstrates that there was a thin SLW layer ~200 m thick at the flight level and that larger ice particles appeared deeper within the cloud below the generating level.

To determine the microphysical properties of GCs, the time series of $Z_e$ from the HCR, total number concentration ($N_t$) from the 2DS ($D > 50$ μm) and 2DC ($D > 150$ μm), the mass mean diameter ($D_m$) from the CDP, the median mass diameter ($D_{mm}$) from the 2DS ($D > 50$ μm) and 2DC ($D > 150$ μm), and the LWC, IWC, and RICE voltage are shown in Figure 4 for the flight leg. The low $\delta_p$ near cloud top (Figure 3c) and the rapid voltage change from the RICE (Figure 4d) demonstrate the continuous presence of SLW along the flight leg. This, combined with the nonspherical images from the 2DS presented in Figure 5, show that some
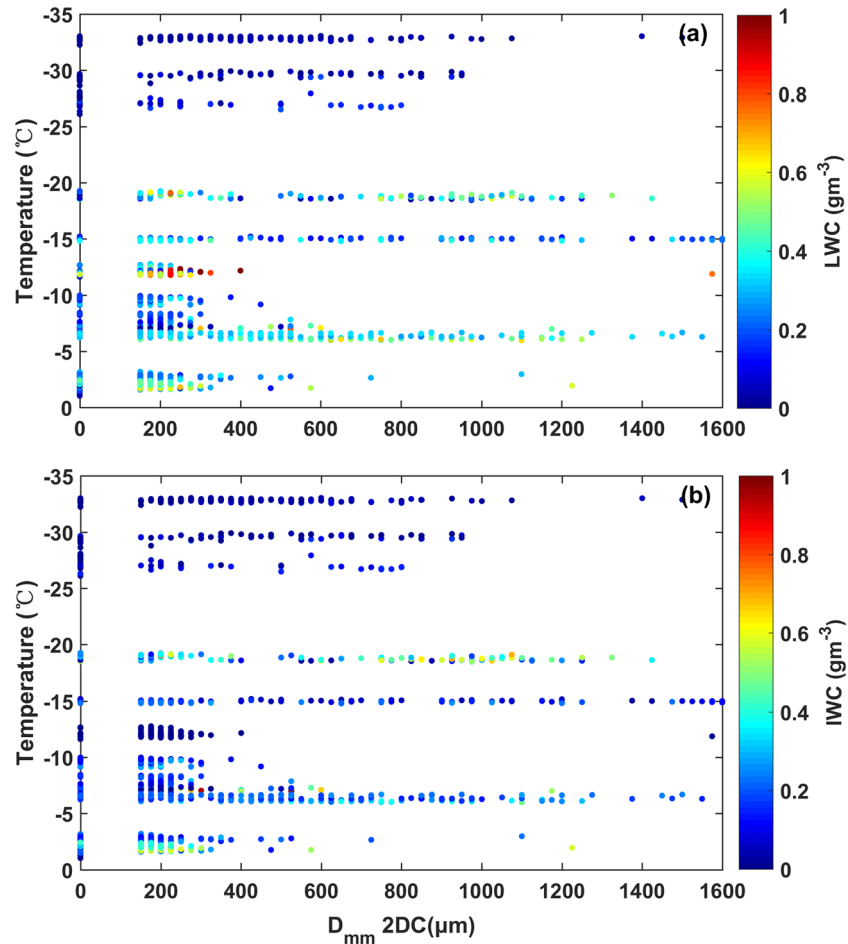
**Figure 13.** All T – $D_{mm}$ data pairs for the full GC regions, colored by (a) LWC and (b) IWC. Each point in the figure is from 1 Hz data.

observations were obtained in mixed-phase conditions. Note that the sawtooth pattern in Figure 4d is caused by the increasing voltage when SLW is freezing on the RICE, with the reduction in voltage occurring when the accreted ice is melted and shed from the probe. Though the phase of some of the smallest 2DS/2DC images cannot be unambiguously identified, there is not any available evidence for the presence of drizzle, and the PHIPS scattering data show that no drizzle drops was present within its range of detection (>60 μm). Thus, the available evidence shows that the larger particles were ice particles. Therefore, particles with $D > 50$ μm are assumed to be ice.

Inspection of Figure 4 demonstrates that there are differences in the microphysical properties inside and outside of the GCs. For example, the CDP $N_t$ frequently peaks in synchronization with the peaks in $Z_e$ (e.g., the specific times at 011034, 011058, and 011205). Other parameters such as the 2DS $N_t$, 2DC $N_t$, LWC, and IWC exhibit some degree of correlation with $Z_e$ with correlation coefficients of 0.32, 0.26, 0.45, and 0.40, respectively (Table 2). Note that $N_t$ at some specific times did not completely correspond to the peaks in $Z_e$ (e.g., 010952 and 011039). This might be caused by the height separation between the in situ cloud probes and radar ($Z_e$ was measured 145 m below the aircraft) with radar data being used to locate th GCs and in situ cloud probes characterizing the microphysical properties. The peaks may be offset because of vertical wind shear. Time periods with lack of correlation might also occur since $N_t$ is dominated by small particles and $Z_e$ dominated by larger particles, and different processes may affect the distribution of each. Any offset, when occurring, was generally not large as the locations of the $Z_e$ and $N_t$ peaks were typically within ±1–2 s, with the $N_t$ peak occurring inside the GCs. The offset is even smaller when the statistical analyses are considered because the offsets of the peaks can be either positive or negative. Table 2 shows the correlation coefficients
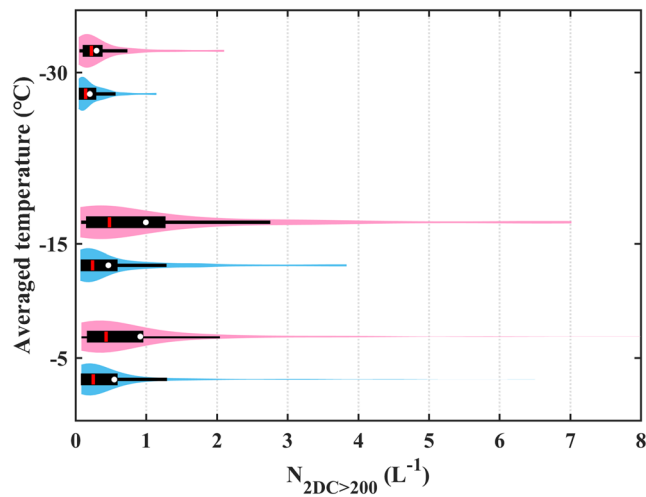
**Figure 14.** Kernel probability density distributions of ice concentration with $D > 200\ \mu m$ from 2DC ($N_{2DC > 200}$) distributions inside (dark red color) and outside GCs (blue color) averaged for three temperature intervals (i.e., −10°C to 0° C, −20°C to −10°C, and −35°C to −25°C). The black boxplots, from left to right, show the 5th, 25th, 50th (red line), 75th, and 95th range of data in each distribution. The white points in boxplots indicate the mean values. The width of red and blue shaded area represents the proportion of the data located there.

of the microphysical properties with $Z_e$ and $w_a$. Both $Z_e$ and $w_a$ are correlated. The correlation coefficients of the microphysical properties with respect to $Z_e$ are higher than those with respect to $w_a$. This might be expected, given that $Z_e$ is related to the sixth moment of the particle size distributions, assuming Rayleigh scattering, and $w_a$ is a relatively independent measure of air velocity.

Figure 6 shows the statistical distributions of the microphysical properties inside and outside of the GCs. Note that the frequency distributions are represented by the violin plots (the shaded red and blue color), which outline the Kernel probability densities, with the width of the shaded area representing the proportion of the data located there (Hintze & Nelson, 1998). Figures 6a and 6b show that the LWC and CDP $N_t$ are larger within GCs than between GCs (passing the significant test for $p < .05$). The median LWC within GCs is 0.036 g m$^{-3}$, with a 25th (75th) percentile of 0.029 g m$^{-3}$ (0.042 g m$^{-3}$). These are ~90% (10%) larger than those between GCs, which have 25th (75th) percentile of LWC of 0.015 g m$^{-3}$ (0.038 g m$^{-3}$). The CDP $N_t$ values show similar trends, with 25th, 50th, and 75th percentiles of 63.5, 73.2, and 80.4 cm$^{-3}$, respectively, within GCs, and smaller values of 35.1, 60.1, and 70.1 cm$^{-3}$ between the GCs. On the other hand, there is no significant difference for the CDP $D_m$ inside GCs compared to outside GCs, with the same median $D_m$ of ~11 μm (Figure 6c).

The number concentration of ice crystals is less than the number concentrations of supercooled water drops. The median 2DC $N_t$ and IWC are 0.18 L$^{-1}$ and 0.04 g m$^{-3}$ (0.11 L$^{-1}$ and 0.03 g m$^{-3}$) for regions inside (outside) the GCs. The median 2DC $N_t$ inside the GCs is 58% larger ($p < .05$) than those outside the GCs, indicating the GC is providing a favorable environment for the formation of ice. Figure 6f further shows that larger ice particles are present inside the GCs compared to regions outside the GCs showing a more favorable environment for the growth of ice. For example, the 25th, 50th, and 75th percentiles of 2DC $D_{mm}$ within GCs are 225, 350, and 506 μm, which are 53% larger on average ($p < .05$) than those between the GCs with corresponding percentiles of 150, 225, and 325 μm. The averaged 2DS $N_t$ ($D_{mm}$), which includes information about particles with $D$ as small as 50 μm (not shown in the figure), is 35% (27%) larger inside the GCs than between the GCs. The relative differences in ice crystal properties inside and outside the GCs are larger than the relative differences in the properties of water droplets. This suggests that small liquid droplets with sizes around 10 μm are being effectively mixed by the turbulence as previously noted by McFarquhar et al. (2011). The small horizontal scales of the GCs increase the effectiveness of the mixing in the SO clouds compared to observations in other geographic regions. Figure 5 shows representative images of particles inside and outside the GCs. There is a mixture of small irregular crystals, bullets, columns, and some larger graupel indicating ice growth occurred by both water vapor deposition and riming. The crystal shapes inside and outside the GCs do not appear to visually differ, but there are larger particles inside the GCs. This shows that the regions inside GCs with stronger updrafts provided a more favorable environment for particle growth by deposition and riming compared with regions outside the GCs as suggested by previous studies (e.g. Plummer et al., 2014; Rosenow et al., 2014).

The very low ice concentrations (less than 0.2 L$^{-1}$ for this case) and the lack of any seeding from above cloud layers (no clouds atop

**Table 3**
*The Statistic Percentage of the Ice Particle Habit From the PHIPS Data for the Entire GC Regions*

| Habit | Percentage |
| --- | --- |
| Small irregular | 26.4 |
| Irregular | 17.6 |
| Column | 9.6 |
| Needle | 8 |
| Side plane | 4 |
| Bullet rosette | 3.2 |
| Hollow column | 2.4 |
| Graupel | 0.8 |
| Skeleton plate | 0 |
| Sheath | 0 |
| Sectored plate | 0 |
| Plate | 0 |
| Frozen droplet | 0 |
| Dendrite | 0 |
| Capped column | 0 |

| Attribute | Percentage |
| --- | --- |
| Rimed | 26.4 |
| Pristine | 1.6 |
| Aggregate | 0 |
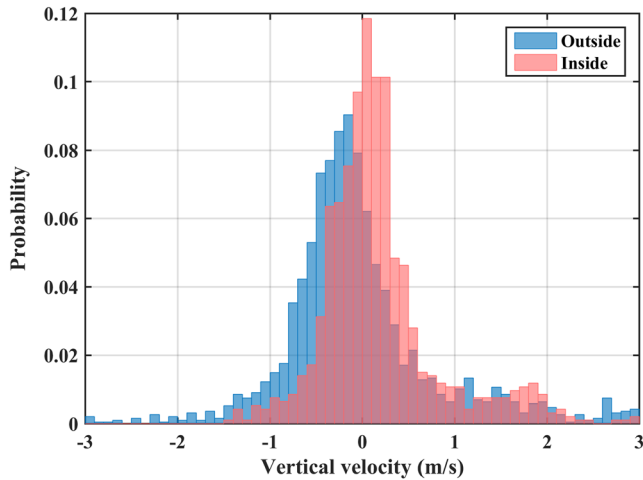
**Figure 15.** The normalized probability functions of $w_a$ inside (red color) and outside the GCs (blue color).

nearby as seen from the images took by the forward-looking camera) indicates that the ice formation process may be explained by heterogeneous nucleation. Since very few ice nucleating particles (INPs) are available over the SO at such low temperatures (DeMott et al., 2016), not much liquid water was depleted. The lack of large water droplets and cold temperatures suggests the Hallett-Mossop process (Hallett & Mossop, 1974) of secondary ice nucleation was not occurring in these GCs. The low INP concentrations and low consumption of SLW thus could be a reason why there is prevalent SLW (see also Table 1) both inside and outside of the GCs at a temperature of $-32.8°C$ for this segment.

### 3.2. Generating Cells at the Top of Boundary Layer Clouds

Figure 7 shows the profile of $Z_e$, W, $\delta_p$, and the time variation of $Z_e$ and W at the first usable radar range gate and aircraft measured $w_a$ at flight level for a 5 min period when the G-V was flying through the tops of boundary clouds at a temperature of $\sim-2°C$ between 031900 and 032400 on 20 February 2018. As for the case of the higher-level cloud, the typical structures of GCs, with enhanced reflectivity at cloud top, fall streaks beneath and fluctuations of vertical velocity at cloud top are evident. The horizontal scale of the GCs ranged from 131 to 918 m with a mean value of 435 m for this segment, comparable to the scales seen in the higher-level cloud on 24 January 2018. The SLW droplet concentrations are larger compared to the higher-layer cloud, with a mean CDP $N_t$ of 150 cm$^{-3}$. Further, Figure 8 shows that drizzle occurs near cloud top with droplets imaged by the PHIPS having $D$ as large as 154 μm. In this case, 35% (0%) of the liquid particles were larger than 150 μm (200 μm) as shown by the PHIPS scattering measurements. Therefore, the number concentation from the 2DS/2DC for particles with $D > 200$ μm (hereafter $N_{2DS > 200}/N_{2DC > 200}$) was used to characterize the ice particle properties for this case as discussed in section 2. Figure 9 shows 2DC images inside and outside the GCs. Despite the limited resolution, it is seen that many particles appear to be supercooled drizzle rather than ice with the identification from PHIPS scattering data. There are also a few large nonspherical particles evident in the images within the GCs. But the averaged $N_{2DS > 200}/N_{2DC > 200}$ in this case was very low (0.07/0.01 L$^{-1}$). Thus, the properties of ice particles will not be discussed in this case.

The time series of CDP $N_t$, $N_{2DC > 200}$, and the number concentration from the 2DS for particles with $50 < D < 200$ μm ($N_{50 < 2DS < 200}$ hereafter) shown in Figure 10 suggest that these properties are correlated with $Z_e$ as seen from the coincidence of peaks in most of the shaded gray regions. For instance, the correlation coefficients between CDP $N_t$, $N_{50 < 2DS < 200}$, and $N_{2DC > 200}$ with $Z_e$ are 0.37, 0.34, and 0.65, respectively, with smaller values of 0.22, 0.23, and 0.56 for the correlations with respect to $w_a$ (Table 2). Figure 11 compares the statistical distributions of the microphysical properties inside and outside the GCs for this boundary layer case. The median value of the CDP $D_m$ is 19.6 μm within GCs and 20.0 μm between GCs (no significant difference, $p > .05$), which is consistent with a lack of correlation of CDP $D_m$ with $Z_e$. But, when examining the sizes and concentrations of particles with $50$ μm $< D < 200$ μm measured by the 2DS, which are indicative of drizzle, larger and more numerous drops are inside the GCs (Figures 11d–11h). The increased number of larger droplets inside the GCs, compared to the those outside the GCs, suggests the growth of droplets is occurring more effectively in the updrafts of the GC regions with the smaller drops being mixed between GC regions due to turbulence. The fact that the GCs are providing a favorable environment for droplet growth is also seen from the significantly larger LWCs in the GCs, with a median value of 0.56 and 0.05 g m$^{-3}$ ($\sim8\%$) larger than LWCs outside the GCs ($p < .05$).
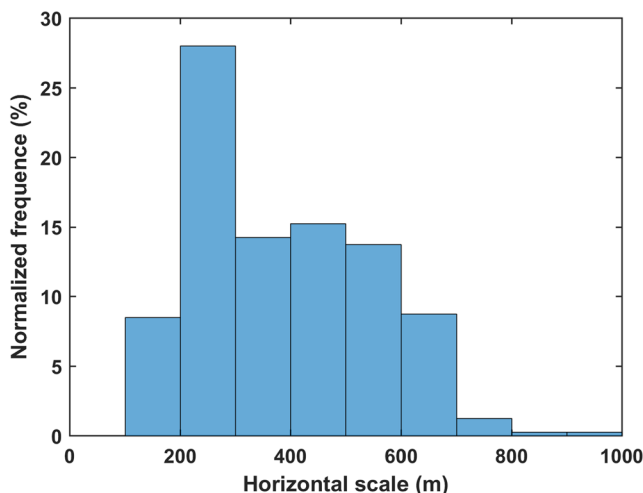


**Figure 16.** The normalized frequency distributions of horizontal width for the full GC data set.
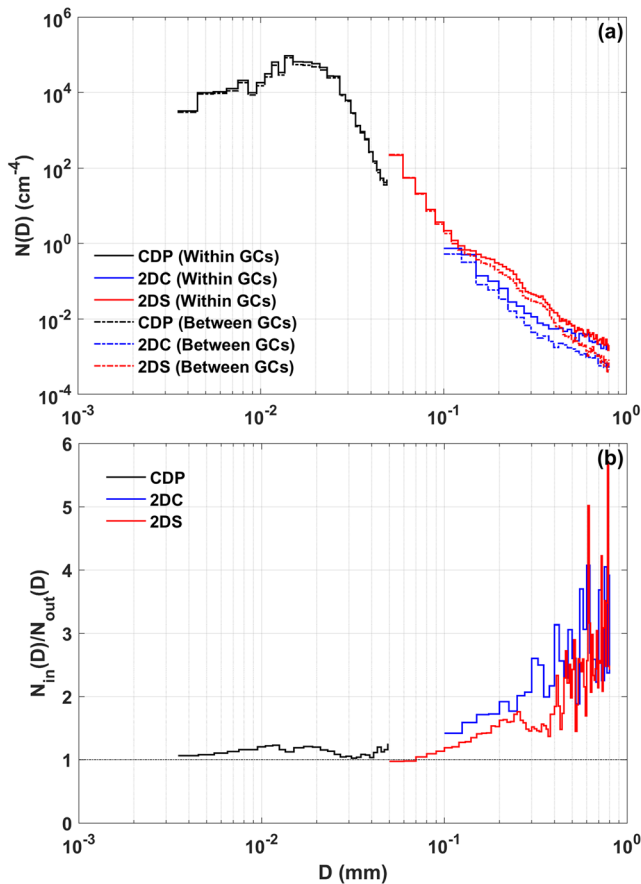
**Figure 17.** As in Figure 12, except averaged for the entire GCs data set.

The ice concentrations and IWCs, on the other hand, are too low in this case to effectively compare values within and outside GCs, as few ice particles occur in the time series of Figure 10a. Nevertheless, the minimal data indicates more large particles are inside than outside the GCs. Figures 11e–11g, which examine the variation of IWC and ice concentrations between the regions, show that many median values are 0, which is reasonable as seen from the time series in Figure 10.

Figure 12 shows the ratio of the average number distribution functions measured inside GCs, $N_{in}(D)$ to average number distribution functions measured between GCs, $N_{out}(D)$ from the CDP, 2DC, and 2DS for this boundary layer case. The CDP exhibits a unimodal distribution with a peak at around 20 μm, regardless of whether observations are inside or between GCs. This peaked distribution is indicative of SLW (McFarquhar & Cober, 2004). On average, the CDP $N(D)$ within the GCs are 17% higher than those between GCs averaged for each size bin. As $D$ increases from 100 to 300 μm, the ratio of $N_{in}(D)/N_{out}(D)$ measured by the 2DS to that measured by the 2DC increases from ~1.5 to 9.5, indicating that more and larger droplets tend to be inside the GCs favored by the updraft environments in GCs.

To summarize, although the ice concentrations were very low for this boundary layer cloud, similar differences in the microphysical properties inside and between the GCs were seen as for the higher altitude cloud. An especially notable difference was the increased number and larger droplets within the GCs than those between them. The next section examines the generality of the findings derived for these two specific clouds by conducting a statistical analysis for all GCs observed during SOCRATES.

## 4. Statistical Analyses for Full GC Data Set

This section summarizes the statistical distributions of the microphysical properties measured within and between GCs. As in section 3, the prominence of $Z_e$ is used to define whether measurements were obtained within or between GCs. Table 1 summarizes the full data set of GCs during SOCRATES, listing the flight time, average altitude and temperature, and presence of SLW/drizzle during each flight. There were 16 cases during SOCRATES when the G-V was flying near cloud top, with the HCR pointed down so that the GC cores could be identified while making simultaneous in-cloud microphysical measurements. Ten out of 15 flights flown during SOCRATES had identifiable GCs that could be used in the analyses. On some flights more than one constant altitude flight leg sampling GCs was performed. Most of the GCs (except for Case no.10) were sampled south of 53°S, and there were four flight legs with GCs observed near 60°S.

All transit legs with HCR data were examined revealing that GCs seldom appear in cumulus clouds, but that GCs in stratus and stratocumulus were frequently observed. Only 16 cases were identified for inclusion in the statistical analysis because the multiple legs flown during SOCRATES to accomplish multiple objectives meant that the needed combination of the G-V flying near cloud top with its radar pointed down only happened a few times on specific flights. The occurrence frequency of GCs varies depending on different cloud types that the G-V sampled. Although there is some uncertainty in exactly how close the measurements were to cloud top, efforts were made to ensure the flight legs were near cloud top, by only using cases when the G-V was descending from above the cloud and thereafter flying near cloud top at a relatively constant altitude. Although the cloud top altitude may change during the constant altitude leg, the variation should be minimal as most GCs are near the tops of the stratocumulus over the SO. For the high-altitude cloud case, the largest variation of cloud top altitude is ~400 m, and most of the clouds sampled are stratiform as shown in Figure 3.
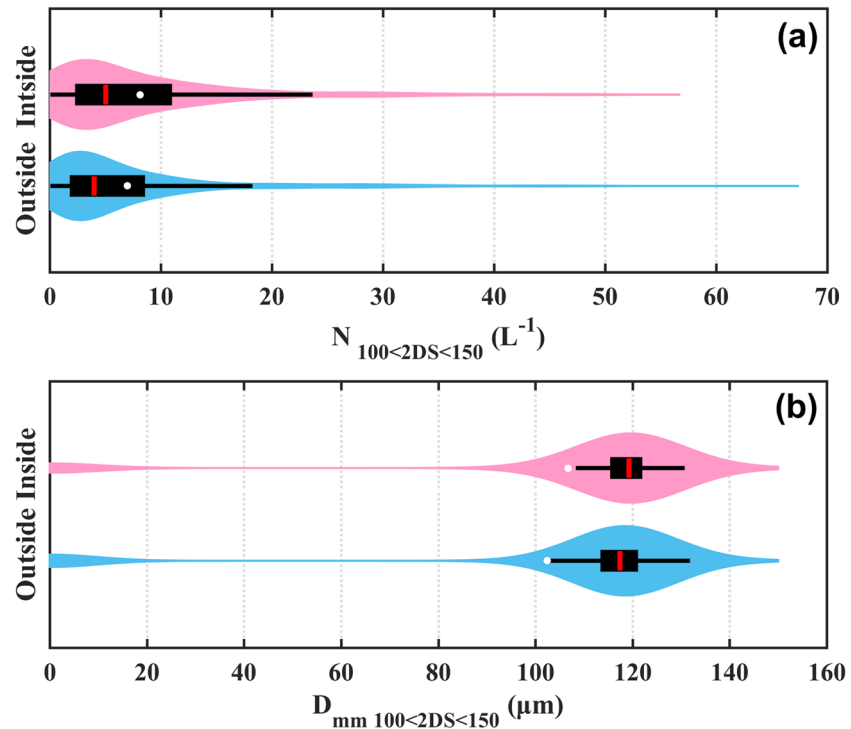
**Figure 18.** Kernel probability density distributions of microphysical properties inside (dark red color) and outside GCs (blue color) for (a) number concentration and (b) mass mean diameter for spherical particles with $100 < D < 150\ \mu m$ when drizzle was present. The black boxplots, from left to right, show the 5th, 25th, 50th (red line), 75th, and 95th range of data in each distribution. The white points in the boxplots indicate the mean values. The width of red and blue shaded area represents the proportion of the data located there.

Table 1 shows that all GC cases were accompanied by the presence of SLW regardless of whether they were above or within the boundary layer. Figure 13 summarizes the 2DC $D_{mm}$ colored by LWC and IWC as a function of temperature for all the cloud top regions both inside and outside GCs. SLW was detected over a wide range of temperatures because depletion of the liquid water by ice was minimal as sampling was near cloud top but warmer than about $-36°C$. SLW was sampled most frequently between $-20$ and $-2°C$, which encompassed the preferred range of in situ sampling where the boundary layer clouds occurred. The G-V typically did not fly at temperatures between $-25°C$ and $-20°C$, as the temperatures of the high-altitude transit legs were lower. Thus, the figure does not provide information on the distribution of LWC/IWC in the temperature range of $-25°C$ to $-20°C$. But, Figure 13 does show that both the LWC and IWC have larger values between $-20$ and $-2°C$ than between $-35$ and $-25°C$, indicating prevalent SLW and relatively high LWC in the boundary layer and stratocumulus cloud-top GC regions during SOCRATES. Note that the $D_{mm}$ shown here mainly corresponds to the presence of ice, at least when $D_{mm} > 200\ \mu m$, since drizzle usually has smaller sizes.

Figure 14 further summaries the ice concentration from 2DC as a function of temperature averaged for three intervals (i.e., $-10°C$ to $0°C$, $-20°C$ to $-10°C$, and $-35°C$ to $-25°C$). It shows that the ice concentration in the cloud top GC regions was typically quite small with the largest ice concentrations between $-20$ to $-10°C$. Though many cases show very small ice concentrations and in some cases the images were too small to get reliable shape information from the optical array probes, habit information is available from the PHIPS for these cases. Table 3 presents the statistical percentage of different ice habits manually identified from the PHIPS stereo-images for all GC regions. It shows that the most frequent ice habits are irregular (44.0%). A large fraction (26.4%) of the ice particles were rimed.

Figure 15 shows the normalized probability functions of $w_a$ inside and outside the GCs. As expected, a clear shift in the distribution is seen with larger velocities inside the GCs compared to outside. The velocities between $-1$ and $1\ m\ s^{-1}$ account for ~81% (75%) of $w_a$ inside (outside) the GCs. The 25th, 50th, and 75th
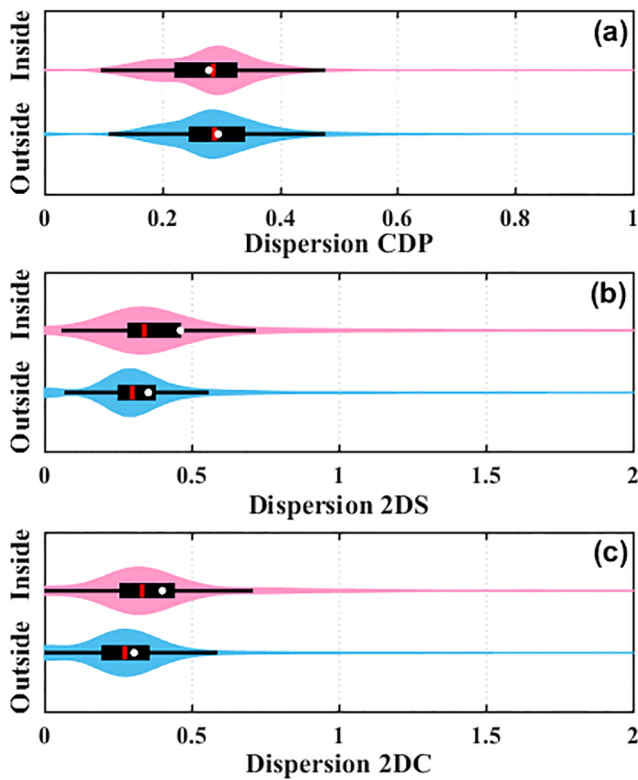
**Figure 19.** Kernel probability density distributions of microphysical properties inside (dark red color) and outside GCs (blue color) for (a) dispersion of CDP $N$(D), (b) dispersion of 2DS $N(D)$, and (c) dispersion of 2DC $N(D)$. The black boxplots, from left to right, show the 5th, 25th, 50th (red line), 75th, and 95th range of data in each distribution. The white points in boxplots indicate the mean values. The width of red and blue shaded area represents the proportion of the data located there.

values within (between) the GCs are −0.18, 0.09, and 0.38 m s$^{-1}$ (−0.50, −0.16, and 0.21 m s$^{-1}$), respectively. The peak normalized probability velocity is −0.15 m s$^{-1}$ between the GCs and is 0.05 m s$^{-1}$ inside the GCs. The slight downward motion outside the GCs compensates the upward motion inside the GCs, ensuring mass conservation.

The horizontal widths of the GCs were calculated based on amount of time the G-V was within the GCs, multiplied by the aircraft true airspeed. Figure 16 shows the normalized frequency distributions of the horizontal width for all GCs sampled during SOCRATES. Overall, 79% of the GCs had horizontal widths between 200 and 600 m. The mean value and standard deviation of the GC widths are 395 and 162 m, respectively, which is smaller than the widths (1–2 km) derived by Rosenow et al. (2014) for midlatitude cyclones. However, Rosenow et al. (2014) examined much deeper circulations than the shallow cloud circulations over the SO, which may be responsible for the difference. In fact, a direct comparison of widths is difficult because different procedures were used to determine width. For example, Plummer et al. (2014) used a 5 s averaged time resolution to identify the GCs rather than the 1 s resolution used in this study, which may also contribute to the smaller GC widths noted here. Further, the estimated horizontal width represents a one-dimensional cross section of a three-dimensional cloud and may not characterize an area-averaged width, especially since the sampling was usually performed in a north-south direction. Uncertainties in the prominence threshold used to identify the GCs could also have introduced uncertainties (~ ±1–2 s) in the identified time within the GCs and hence the widths. Nevertheless, it is clear that the estimated horizontal widths of GCs sampled during SOCRATES are smaller than those of previous projects.

Figure 17 shows the ratio of average $N_{in}(D)$ to $N_{out}(D)$ from the CDP, 2DC, and 2DS for the entire GC data set. Overall, the $N(D)$ within the GCs are larger than those between GCs. For example, the $N_{in}(D)$ for the CDP inside the GCs are ~3–25% higher than those $N_{out}(D)$. As $D$ increases, the differences become larger, especially for particles with $D > 150$ μm measured by the 2DC and 2DS. The ratio of $N_{in}(D)/N_{out}(D)$ increases from about 1.5 to 5 as $D$ increases from 150 to 800 μm. Note that $N(D)$ for $D > 800$ μm is not shown in the plot as only ~8% particles are larger than 800 μm for the entire GC data set. It is not surprising that there is the largest difference within and between GCs on the sizes and concentrations of the largest particles since the $Z_e$, which is dominated by the contributions of the largest particles, was used to determine the location of the GCs. Figure 18 shows the statistical results of $N_{100 < 2DS < 150}$ and $D_{m\ 100 < 2DS < 150}$ only for spherical particles when drizzle was present. The averaged $N_{100 < 2DS < 150}$ and $D_{m\ 100 < 2DS < 150}$ inside the GCs are 5.7 L$^{-1}$ and 107 μm, ~26% and 5% larger ($p < 0.05$) than the values between the GCs. This suggests that the GCs consistently provide a productive environment where more drizzle-sized drops can effectively grow even though there is not a large difference in the sizes of the drops.

Figure 19 examines the dispersion (the ratio of the standard deviation to the mean value) of $N_{in}(D)$ and $N_{out}(D)$, where the size distributions include contributions from ice and liquid particles. The mean (median) values for the 2DS and 2DC dispersions within the GCs are 0.48 and 0.41 (0.34 and 0.34), ~32% (18%) larger than those between the GCs ($p < .05$ for both 2DS and 2DC), showing wider distributions within the GCs. This, combined with $N_{in}(D) > N_{out}(D)$ suggests the ice particle growth inside the GCs may lead to the wider size distributions. By contrast, the SLW distributions show that the mean CDP dispersion is significantly ~6% smaller ($p < .05$) within the GCs than between them, indicating a slightly narrower CDP distribution within the GCs. The narrower distribution of the droplets is caused by condensation growth favored within the updraft, which has been shown in many previous observations and simulations (e.g., Brenguier, 1991; Houghton, 1938; Korolev et al., 2013). Another important dynamic factor that may influence the CDP
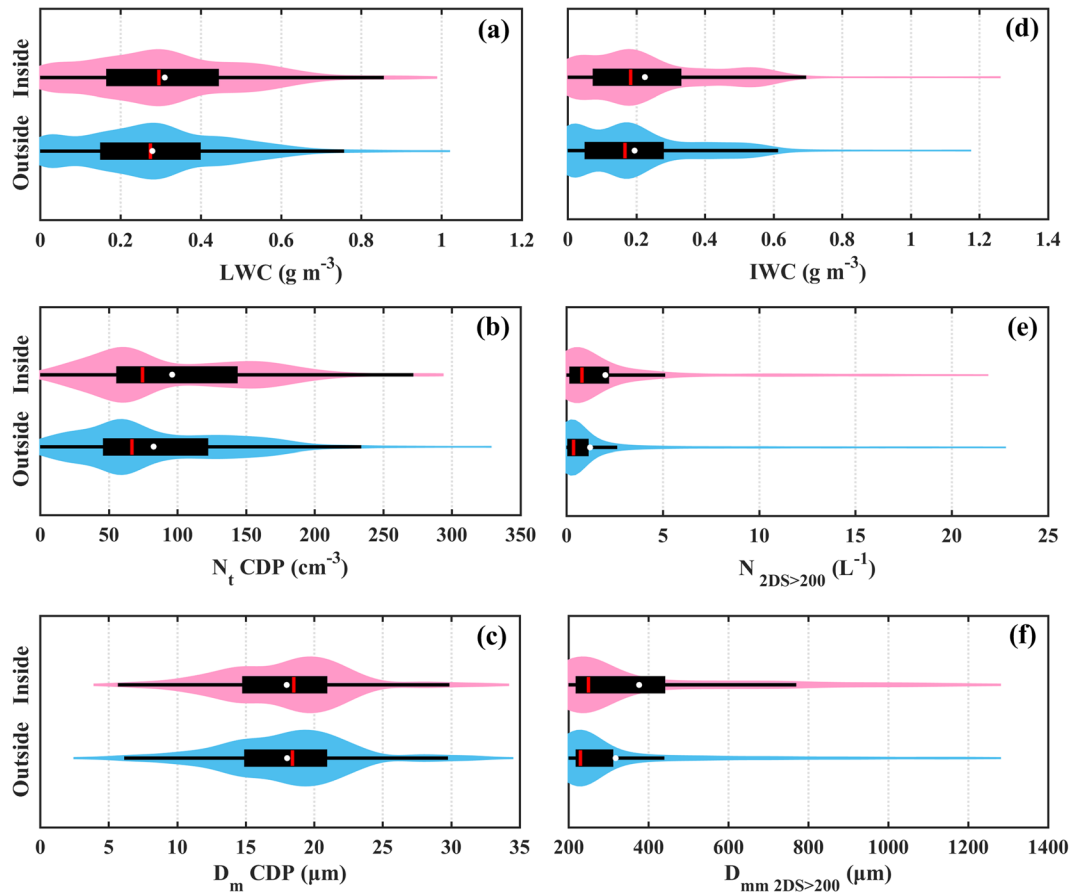
**Figure 20.** (a–d) are the same as Figure 7 but for the entire GC data set. (e) and (f) show the number concentration and median mass diameter for particles with $D > 200$ μm.

distribution is entrainment mixing. However, its effect is not clear because some studies claim entrainment can increase dispersion due to evaporation (Lu et al., 2013; Tölle & Krueger, 2014), while others found a negative correlation between entrainment rate and dispersion (Guo et al., 2018; Lasher-Trapp et al., 2005). Finally, the broadening due to the instrument response from CDP (McFarquhar et al., 2017) might also influence the result shown in Figure 19a. Nevertheless, the slightly different CDP dispersions inside and outside the GCs suggest that turbulent mixing has a role in making the distribution difference small when comparing points inside and outside GCs as discussed above.

Figure 20 compares the statistical distributions of cloud microphysical properties for regions within and between GCs. Compared to the specific cases discussed in section 3, the differences between properties inside and outside the GCs are smaller. Nevertheless, the differences are still statistically significant except for the differences in CDP $D_m$. The mean and median LWC within (between) the GCs are 0.31 and 0.29 g m$^{-3}$ (0.28 and 0.27 g m$^{-3}$), respectively, ranging from the 25th to 75th percentiles of 0.17 to 0.45 g m$^{-3}$ (0.15 to 0.41 g m$^{-3}$). These LWC values averaged ~0.03 g m$^{-3}$ (~11%) larger within compared to between the GCs. The IWC also shows statistically significant differences, with averages of ~0.03 g m$^{-3}$ (~15%) larger within, compared to between the GCs. Considering the inhomogeneities and small-scale structure of the GCs, this small difference suggests that turbulence inherent to the GC regions acted to mix air masses inside and outside the GCs in meteorological situations similar to those observed by others (Field et al., 2004; McFarquhar et al., 2011). Thus, the mixing process may play a role in minimizing the differences within and between the GCs over time.

The 25th, 50th, 75th, and the mean values of total number concentrations from the CDP within (between) the GCs are 56.1, 74.7, 143.3, and 96.1 cm$^{-3}$ (46.4, 66.9, 121.9, and 82.8 cm$^{-3}$), respectively, showing values 12–21% larger inside GCs compared to between GCs. Figures 20e and 20f show the statistically significant

differences of 2DS number concentration and $D_{mm}$ within and between GCs for ice particles ($D > 200$ μm). In contrast to the CDP $N_t$, the $N_{2DS > 200}$ have larger differences within and between the GCs. The mean number concentration, 25th, 50th, and 75th percentiles are 2.0, 0.2, 0.8, and 2.0 $L^{-1}$, respectively, averaged within the GCs. These are 65–220% larger than those between the GCs. For $D_{mm\ 2DS > 200}$, the mean value within the GCs is 323 μm, which is 37% larger than between GCs. The 25th to 75th percentiles of the $D_{mm\ 2DS > 200}$ within the GCs are 9% to 42% larger than between them. These microphysical properties were also inspected as a function of temperature (figure not shown), and the results for the differences between the SLW and ice particle properties are similar regardless of the temperature range. In general, the increasing differences in particle concentration with increasing size establish that more and larger ice particles are inside the GCs.

The thermodynamic properties (e.g., temperature, dew point, and potential temperature) inside and outside the GCs (figure not shown), however, were found to not be significantly different. It is not surprising that there is little difference between the thermodynamic values inside and outside of the GCs given the small horizontal dimensions of the GCs and the mixing and entrainment processes that are acting.

In summary, more and larger ice particles were observed inside the small-scale GCs compared to outside the GCs. The GC regions also had enhanced presence of SLW but smaller differences for the number concentration and sizes of droplets inside compared regions between the GCs.

## 5. Conclusions

In this study a first characterization of ubiquitous generating cells (GCs) observed over the Southern Ocean (SO) during the Southern Ocean Clouds Radiation Aerosol Transport Experimental Study (SOCRATES) is presented. The microphysical properties within and between the GCs, measured by a suite of in-situ cloud probes onboard the G-V aircraft, are characterized and compared to show how the bulk properties and number distribution functions of cloud supercooled liquid water (SLW) and ice varied inside and between GCs. The GC locations were identified by applying an improved algorithm based on radar reflectivity factor measured by the HCR. Sixteen cases were analyzed when the G-V was flying inside and between the GCs near cloud top, with the HCR pointed down; the cases were selected so that coincident information on the reflectivity cores and microphysical properties were available. Further, two cases studies of GCs, one observed in a high-level cloud and the other a boundary layer cloud, were analyzed in detail to provide more information about processes occurring in GCs. The principal findings of this study are summarized as follows:

1. SLW was detected within all the GCs over the SO, even at temperatures as low as −33°C. The average LWC within the GCs sampled was 0.31 ± 0.19 g $m^{-3}$, which was 11% larger on average than values observed between the GCs. The CDP $N_t$ averaged for periods inside the GCs was 96.1 ± 58.3 $cm^{-3}$, 16% larger than values averaged for periods outside the GCs. But the mass mean diameter ($D_m$) of the cloud droplets measured by the CDP was not significantly different inside and between the GCs. The small difference inside and between the GCs might be caused by the weak depletion due to lack of ice nucleating particles and thus low ice particle concentrations, as well as the turbulence inherent in the GCs, which acted to mix the SLW throughout the GC regions.
2. The *N(D)* for ice particles inside the GCs for $D > 200$ μm was 2.0 ± 3.3 $L^{-1}$, 65% larger than those outside GCs on average. As *D* increased, this percentage difference became larger (~150% to 500%). The median mass diameter, $D_{mm}$, was 323 ± 263 μm, 37% larger within than outside GCs on average. Combined with the narrower distributions of the droplets and increased number and size of larger drops/drizzles within the GCs, this suggests that the regions inside the GCs with stronger updrafts provided a favorable environment for simultaneous growth of SLW and ice particles compared to regions outside the GCs.
3. The horizontal width for most GCs observed over the SO ranged from 200 to 600 m. The mean value and standard deviation were 395 and 162 m, respectively, much smaller than the widths computed by Rosenow et al. (2014) for winter cyclones over the midwestern United States.

The small horizontal scales of the GCs, and their turbulent nature (evident from the close proximity of updrafts and downdrafts and the ubiquity of SLW both inside and outside the GC regions), suggest that turbulence inherent to the GC regions is causing mixing to occur within and between the GCs. This is consistent with observations analyzed by Field et al. (2004) and McFarquhar et al. (2011) in other meteorological

situations. Therefore, while the uncertainties of the method in identifying GC locations impact the results, the measurements also suggest the importance of turbulent mixing acting to lessen the observed differences inside and outside the GCs. Therefore, the small horizontal scales of GCs, the possible roles of GCs on the distribution of SLW and ice particle mass, and GC impacts on radiation and precipitation should be taken into consideration to provide better simulations of SO clouds.

### Data Availability Statement

The data that support the findings of this study are available online (https://data.eol.ucar.edu/master_list/? project=SOCRATES).

### References

Abdelmonem, A., Järvinen, E., Duft, D., Hirst, E., Vogt, S., Leisner, T., & Schnaiter, M. (2016). PHIPS-HALO: The airborne particle habit imaging and polar scattering probe-part 1: Design and operation. *Atmospheric Measurement Techniques*, *9*(7), 3131–3144. https://doi. org/10.5194/amt-9-3131-2016

American Meteorological Society (2013). Generating cell Glossary of Meteorology. Retrieved from http://glossary.ametsoc.org/wiki/generating_cell

Baker, B., & Lawson, R. P. (2006). Improvement in determination of ice water content from two-dimensional particle imagery. Part I: Image-to-mass relationships. *Journal of Applied Meteorology and Climatology*, *45*(9), 1282–1290. https://doi.org/10.1175/JAM2398.1

Baumgardner, D., Abel, S., Axisa, D., Cotton, R., Crosier, J., Field, P., et al. (2017). Cloud ice properties: In situ measurement challenges. *Meteorological Monographs*, *58*, 9.1–9.23. https://doi.org/10.1175/AMSMONOGRAPHS-D-16-0011.1

Baumgardner, D., & Korolev, A. (1997). Airspeed corrections for optical array probe sample volumes. *Journal of Atmospheric and Oceanic Technology*, *14*(5), 1224–1229. https://doi.org/10.1175/1520-0426(1997)014<1224:ACFOAP>2.0.CO;2

Bergeron, T. (1950). Über der mechanismus der ausgeibigen Niederschläge. *Berichte der Deutschen Wetterdienstes*, *12*, 225–232.

Brenguier, J. L. (1991). Parameterization of the condensation process: A theoretical approach. *Journal of the Atmospheric Sciences*, *48*(2), 264–282. https://doi.org/10.1175/1520-0469(1991)048<0264:POTCPA>2.0.CO;2

Browning, K. (1983). Air motion and precipitation growth in a major snowstorm. *Quarterly Journal of the Royal Meteorological Society*, *109*(459), 225–242. https://doi.org/10.1002/qj.49710945911

Carbone, R., & Bohne, A. R. (1975). Cellular snow generation—A Doppler radar study. *Journal of the Atmospheric Sciences*, *32*(7), 1384–1394. https://doi.org/10.1175/1520-0469(1975)032<1384:CSGDRS>2.0.CO;2

Cober, S. G., Isaac, G. A., Korolev, A. V., & Strapp, J. W. (2001). Assessing cloud-phase conditions. *Journal of Applied Meteorology*, *40*(11), 1967–1983. https://doi.org/10.1175/1520-0450(2001)040<1967:ACPC>2.0.CO;2

Crosier, J., Choularton, T., Westbrook, C., Blyth, A., Bower, K., Connolly, P., et al. (2014). Microphysical properties of cold frontal rainbands. *Quarterly Journal of the Royal Meteorological Society*, *140*(681), 1257–1268. https://doi.org/10.1002/qj.2206

Cunningham, J. G., & Yuter, S. E. (2014). Instability characteristics of radar-derived mesoscale organization modes within cool-season precipitation near Portland, Oregon. *Monthly Weather Review*, *142*(5), 1738–1757. https://doi.org/10.1175/MWR-D-13-00133.1

DeMott, P. J., Hill, T. C., McCluskey, C. S., Prather, K. A., Collins, D. B., Sullivan, R. C., et al. (2016). Sea spray aerosol as a unique source of ice nucleating particles. *Proceedings of the National Academy of Sciences of the United States of America*, *113*(21), 5797–5803. https://doi. org/10.1073/pnas.1514034112

Dorsi, S., Kalnajs, L., Toohey, D., & Avallone, L. (2014). A fiber-coupled laser hygrometer for airborne total water measurement. *Atmospheric Measurement Techniques*, *7*(1), 215–223. https://doi.org/10.5194/amt-7-215-2014

Dorsi, S. W. (2013). *Airborne and surface-level in situ observations of wintertime clouds in the southern Rockies* (PhD thesis, 189 pp.). University of Colorado at Boulder. https://scholar.colorado.edu/concern/graduate_thesis_or_dissertations/5m60qs02z

Douglas, R. H., Gunn, K. L. S., & Marshall, J. S. (1957). Pattern in the vertical of snow generation. *Journal of Meteorology*, *14*(2), 95–114. https://doi.org/10.1175/1520-0469(1957)014<0095:PITVOS>2.0.CO;2

Ellis, S., Loew, E., Burghart, C., Tsai, P. S., Dixon, M. J., Emmett, J. M., et al. (2017). Use of the Earth's surface as a reference to correct airborne radar radial velocity measurements for platform motion. 38th Conference on Radar Meteorology, 23 August–1 September 2017, Chicago IL.

Evans, A. G., Locatelli, J. D., Stoelinga, M. T., & Hobbs, P. V. (2005). The IMPROVE-1 storm of 1–2 February 2001. Part II: Cloud structures and the growth of precipitation. *Journal of the Atmospheric Sciences*, *62*(10), 3456–3473. https://doi.org/10.1175/JAS3547.1

Field, P., Heymsfield, A., & Bansemer, A. (2006). Shattering and particle interarrival times measured by optical array probes in ice clouds. *Journal of Atmospheric and Oceanic Technology*, *23*(10), 1357–1371. https://doi.org/10.1175/JTECH1922.1

Field, P., Hogan, R., Brown, P., Illingworth, A., Choularton, T., Kaye, P. H., et al. (2004). Simultaneous radar and aircraft observations of mixed-phase cloud at the 100 m scale. *Quarterly Journal of the Royal Meteorological Society*, *130*(600), 1877–1904. https://doi.org/ 10.1256/qj.03.102

Gunn, K., Langleben, M., Dennis, A., & Power, B. (1954). Radar evidence of a generating level for snow. *Journal of Meteorology*, *11*(1), 20–26. https://doi.org/10.1175/1520-0469(1954)011<0020:REOAGL>2.0.CO;2

Guo, X., Zhao, T., Liu, Y., Zhang, G. J., & Luo, S. (2018). Observational study of the relationship between entrainment rate and relative dispersion in deep convective clouds. *Atmospheric Research*, *199*, 186–192. https://doi.org/10.1016/j.atmosres.2017.09.013

Hallett, J., & Mossop, S. C. (1974). Production of secondary ice particles during the riming process. *Nature*, *249*(5452), 26–28. https://doi. org/10.1038/249026a0

Haynes, J. M., Jakob, C., Rossow, W. B., Tselioudis, G., & Brown, J. (2011). Major characteristics of Southern Ocean cloud regimes and their effects on the energy budget. *Journal of Climate*, *24*(19), 5061–5080. https://doi.org/10.1175/2011JCLI4052.1

Herzegh, P. H., & Hobbs, P. V. (1980). The mesoscale and microscale structure and organization of clouds and precipitation in midlatitude cyclones. II: Warm-frontal clouds. *Journal of the Atmospheric Sciences*, *37*(3), 597–611. https://doi.org/10.1175/1520-0469(1980) 037<0597:TMAMSA>2.0.CO;2

Heymsfield, A. (1975a). Cirrus uncinus generating cells and the evolution of cirriform clouds. Part II: The structure and circulations of the cirrus uncinus generating head. *Journal of the Atmospheric Sciences*, *32*(4), 809–819. https://doi.org/10.1175/1520-0469(1975)032<0809: CUGCAT>2.0.CO;2

Heymsfield, A. (1975b). Cirrus uncinus generating cells and the evolution of cirriform clouds. Part I: Aircraft observations of the growth of the ice phase. *Journal of the Atmospheric Sciences*, *32*(4), 799–808. https://doi.org/10.1175/1520-0469(1975)032<0799:CUGCAT>2.0. CO;2

Heymsfield, A. (1975c). Cirrus uncinus generating cells and the evolution of cirriform clouds. Part III: Numerical computations of the growth of the ice phase. *Journal of the Atmospheric Sciences*, *32*(4), 820–830. https://doi.org/10.1175/1520-0469(1975)032<0820: CUGCAT>2.0.CO;2

Heymsfield, A. J., & Parrish, J. L. (1978). A computational technique for increasing the effective sampling volume of the PMS two-dimensional particle size spectrometer. *Journal of Applied Meteorology*, *17*(10), 1566–1572. https://doi.org/10.1175/1520-0450(1978) 017<1566:ACTFIT>2.0.CO;2

Hintze, J. L., & Nelson, R. D. (1998). Violin plots: A box plot-density trace synergism. *The American Statistician*, *52*, 181–184.

Hobbs, P. V., & Locatelli, J. D. (1978). Rainbands, precipitation cores and generating cells in a cyclonic storm. *Journal of the Atmospheric Sciences*, *35*(2), 230–241.

Holroyd, E. W. III (1987). Some techniques and uses of 2D-C habit classification software for snow particles. *Journal of Atmospheric and Oceanic Technology*, *4*(3), 498–511. https://doi.org/10.1175/1520-0426(1987)004<0498:STAUOC>2.0.CO;2

Houghton, H. G. (1938). Problems connected with the condensation and precipitation processes in the atmosphere. *Bulletin of the American Meteorological Society*, *19*(4), 152–159. https://doi.org/10.1175/1520-0477-19.4.152

Houze, R. A. Jr., Rutledge, S. A., Matejka, T. J., & Hobbs, P. V. (1981). The mesoscale and microscale structure and organization of clouds and precipitation in midlatitude cyclones. III: Air motions and precipitation growth in a warm-frontal rainband. *Journal of the Atmospheric Sciences*, *38*(3), 639–649. https://doi.org/10.1175/1520-0469(1981)038<0639:TMAMSA>2.0.CO;2

Hu, Y., Winker, D., Vaughan, M., Lin, B., Omar, A., Trepte, C., et al. (2009). CALIPSO/CALIOP cloud phase discrimination algorithm. *Journal of Atmospheric and Oceanic Technology*, *26*(11), 2293–2309. https://doi.org/10.1175/2009JTECHA1280.1

Huang, Y., Protat, A., Siems, S. T., & Manton, M. J. (2015). A-train observations of maritime midlatitude storm-track cloud systems: Comparing the Southern Ocean against the North Atlantic. *Journal of Climate*, *28*(5), 1920–1939. https://doi.org/10.1175/JCLI-D-14-00169.1

Huang, Y., Siems, S. T., Manton, M. J., Hande, L. B., & Haynes, J. M. (2012). The structure of low-altitude clouds over the Southern Ocean as seen by CloudSat. *Journal of Climate*, *25*(7), 2535–2546. https://doi.org/10.1175/JCLI-D-11-00131.1

Ikeda, K., Rasmussen, R. M., Hall, W. D., & Thompson, G. (2007). Observations of freezing drizzle in extratropical cyclonic storms during IMPROVE-2. *Journal of the Atmospheric Sciences*, *64*(9), 3016–3043. https://doi.org/10.1175/JAS3999.1

Keeler, J. M., Jewett, B. F., Rauber, R. M., McFarquhar, G. M., Rasmussen, R. M., Xue, L., et al. (2016a). Dynamics of cloud-top generating cells in winter cyclones. Part I: Idealized simulations in the context of field observations. *Journal of the Atmospheric Sciences*, *73*(4), 1507–1527. https://doi.org/10.1175/JAS-D-15-0126.1

Keeler, J. M., Jewett, B. F., Rauber, R. M., McFarquhar, G. M., Rasmussen, R. M., Xue, L., et al. (2016b). Dynamics of cloud-top generating cells in winter cyclones. Part II: Radiative and instability forcing. *Journal of the Atmospheric Sciences*, *73*(4), 1529–1553. https://doi.org/ 10.1175/JAS-D-15-0127.1

Keeler, J. M., Rauber, R. M., Jewett, B. F., McFarquhar, G. M., Rasmussen, R. M., Xue, L., et al. (2017). Dynamics of cloud-top generating cells in winter cyclones. Part III: Shear and convective organization. *Journal of the Atmospheric Sciences*, *74*(9), 2879–2897. https://doi. org/10.1175/JAS-D-16-0314.1

King, W., Dye, J., Baumgardner, D., Strapp, J., & Huffman, D. (1985). Icing wind tunnel tests on the CSIRO liquid water probe. *Journal of Atmospheric and Oceanic Technology*, *2*(3), 340–352. https://doi.org/10.1175/1520-0426(1985)002<0340:IWTTOT>2.0.CO;2

King, W., Parkin, D., & Handsworth, R. (1978). A hot-wire liquid water device having fully calculable response characteristics. *Journal of Applied Meteorology*, *17*(12), 1809–1813. https://doi.org/10.1175/1520-0450(1978)017<1809:AHWLWD>2.0.CO;2

Korolev, A. (2007). Reconstruction of the sizes of spherical particles from their shadow images. Part I: Theoretical considerations. *Journal of Atmospheric and Oceanic Technology*, *24*(3), 376–389. https://doi.org/10.1175/JTECH1980.1

Korolev, A., Pinsky, M., & Khain, A. (2013). A new mechanism of droplet size distribution broadening during diffusional growth. *Journal of the Atmospheric Sciences*, *70*(7), 2051–2071. https://doi.org/10.1175/JAS-D-12-0182.1

Kumjian, M. R., Rutledge, S. A., Rasmussen, R. M., Kennedy, P. C., & Dixon, M. (2014). High-resolution polarimetric radar observations of snow-generating cells. *Journal of Applied Meteorology and Climatology*, *53*(6), 1636–1658. https://doi.org/10.1175/JAMC-D-13-0312.1

Langleben, M. P. (1956). The plan pattern of snow echoes at the generating level. *Journal of Meteorology*, *13*(6), 554–560. https://doi.org/ 10.1175/1520-0469(1956)013<0554:TPPOSE>2.0.CO;2

Lasher-Trapp, S. G., Cooper, W. A., & Blyth, A. M. (2005). Broadening of droplet size distributions from entrainment and mixing in a cumulus cloud. *Quarterly Journal of the Royal Meteorological Society*, *131*(605), 195–220. https://doi.org/10.1256/qj.03.199

Lu, C., Niu, S., Liu, Y., & Vogelmann, A. M. (2013). Empirical relationship between entrainment rate and microphysics in cumulus clouds. *Geophysical Research Letters*, *40*, 2333–2338. https://doi.org/10.1002/grl.50445

Marshall, J. S. (1953). Precipitation trajectories and patterns. *Journal of Meteorology*, *10*(1), 25–29. https://doi.org/10.1175/1520-0469(1953) 010<0025:PTAP>2.0.CO;2

Matejka, T. J., Houze, R. A., & Hobbs, P. V. (1980). Microphysics and dynamics of clouds associated with mesoscale rainbands in extra-tropical cyclones. *Quarterly Journal of the Royal Meteorological Society*, *106*(447), 29–56. https://doi.org/10.1002/qj.49710644704

McFarquhar, G. M., Baumgardner, D., Bansemer, A., Abel, S. J., Crosier, J., French, J., & Um, J. (2017). Processing of ice cloud in situ data collected by bulk water, scattering, and imaging probes: Fundamentals, uncertainties, and efforts toward consistency. *Meteorological Monographs*, *58*, 11–11.

McFarquhar, G. M., & Cober, S. G. (2004). Single-scattering properties of mixed-phase Arctic clouds at solar wavelengths: Impacts on radiative transfer. *Journal of Climate*, *17*(19), 3799–3813. https://doi.org/10.1175/1520-0442(2004)017<3799:SPOMAC>2.0.CO;2

McFarquhar, G. M., Finlon, J. A., Stechman, D. M., Wu, W., Jackson, R. C., & Freer, M. (2018). University of Illinois/Oklahoma optical Array probe (OAP) processing software. https://doi.org/10.5281/zenodo.1285969

McFarquhar, G. M., Ghan, S., Verlinde, J., Korolev, A., Strapp, J. W., Schmid, B., et al. (2011). Indirect and semi-direct aerosol campaign: The impact of Arctic aerosols on clouds. *Bulletin of the American Meteorological Society*, *92*(2), 183–201. https://doi.org/10.1175/ 2010BAMS2935.1

McFarquhar, G. M., Zhang, G., Poellot, M. R., Kok, G. L., McCoy, R., Tooman, T., et al. (2007). Ice properties of single-layer stratocumulus during the Mixed-Phase Arctic Cloud Experiment: 1. Observations. *Journal of Geophysical Research*, *112*, D24201. https://doi.org/ 10.1029/2007JD008633

Naud, C. M., Booth, J. F., & Del Genio, A. D. (2014). Evaluation of ERA-Interim and MERRA cloudiness in the Southern Ocean. *Journal of Climate*, *27*(5), 2109–2124. https://doi.org/10.1175/JCLI-D-13-00432.1

Plummer, D. M., McFarquhar, G. M., Rauber, R. M., Jewett, B. F., & Leon, D. C. (2014). Structure and statistical analysis of the micro-physical properties of generating cells in the comma head region of continental winter cyclones. *Journal of the Atmospheric Sciences*, *71*(11), 4181–4203. https://doi.org/10.1175/JAS-D-14-0100.1

Plummer, D. M., McFarquhar, G. M., Rauber, R. M., Jewett, B. F., & Leon, D. C. (2015). Microphysical properties of convectively generated fall streaks within the stratiform comma head region of continental winter cyclones. *Journal of the Atmospheric Sciences*, *72*(6), 2465–2483. https://doi.org/10.1175/JAS-D-14-0354.1

Rauber, R. M., Macomber, M. K., Plummer, D. M., Rosenow, A. A., McFarquhar, G. M., Jewett, B. F., et al. (2014). Finescale radar and airmass structure of the comma head of a continental winter cyclone: The role of three airstreams. *Monthly Weather Review*, *142*(11), 4207–4229. https://doi.org/10.1175/MWR-D-14-00057.1

Rauber, R. M., Plummer, D. M., Macomber, M. K., Rosenow, A. A., McFarquhar, G. M., Jewett, B. F., et al. (2015). The role of cloud-top generating cells and boundary layer circulations in the finescale radar structure of a winter cyclone over the Great Lakes. *Monthly Weather Review*, *143*(6), 2291–2318. https://doi.org/10.1175/MWR-D-14-00350.1

Rauber, R. M., & Tokay, A. (1991). An explanation for the existence of supercooled water at the top of cold clouds. *Journal of the Atmospheric Sciences*, *48*(8), 1005–1023. https://doi.org/10.1175/1520-0469(1991)048<1005:AEFTEO>2.0.CO;2

Rauber, R. M., Wegman, J., Plummer, D. M., Rosenow, A. A., Peterson, M., McFarquhar, G. M., et al. (2014). Stability and charging characteristics of the comma head region of continental winter cyclones. *Journal of the Atmospheric Sciences*, *71*(5), 1559–1582. https://doi.org/10.1175/JAS-D-13-0253.1

Rosenow, A. A., Plummer, D. M., Rauber, R. M., McFarquhar, G. M., Jewett, B. F., & Leon, D. (2014). Vertical velocity and physical structure of generating cells and convection in the comma head region of continental winter cyclones. *Journal of the Atmospheric Sciences*, *71*(5), 1538–1558. https://doi.org/10.1175/JAS-D-13-0249.1

Rutledge, S. A., & Hobbs, P. (1983). The mesoscale and microscale structure and organization of clouds and precipitation in midlatitude cyclones. VIII: A model for the "seeder-feeder" process in warm-frontal rainbands. *Journal of the Atmospheric Sciences*, *40*(5), 1185–1206. https://doi.org/10.1175/1520-0469(1983)040<1185:TMAMSA>2.0.CO;2

Schnaiter, M. (2018). PHIPS-HALO Stereo Imaging Data. Version 1.0 (Version 1.0) [Data set]. UCAR/NCAR - Earth Observing Laboratory. https://doi.org/10.5065/d62b8wwf. Accessed 09 Apr 2019.

Schnaiter, M., Järvinen, E., Ahmed, A., & Leisner, T. (2018). PHIPS-HALO: The airborne particle habit imaging and polar scattering probe–Part 2: Characterization and first results. *Atmospheric Measurement Techniques*, *11*(1), 341–357. https://doi.org/10.5194/amt-11-341-2018

Schultz, D. M., Arndt, D. S., Stensrud, D. J., & Hanna, J. W. (2004). Snowbands during the cold-air outbreak of 23 January 2003. *Monthly Weather Review*, *132*(3), 827–842. https://doi.org/10.1175/1520-0493(2004)132<0827:SDTCOO>2.0.CO;2

Tölle, M. H., & Krueger, S. K. (2014). Effects of entrainment and mixing on droplet size distributions in warm cumulus clouds. *Journal of Advances in Modeling Earth Systems*, *6*, 281–299. https://doi.org/10.1002/2012MS000209

Toohey, D., & Rainwater, B. (2019). NSF/NCAR GV HIAPER CLH-2 Condensed Water Contents Data. Version 1.0 (Version 1.0) [Data set]. UCAR/NCAR - Earth Observing Laboratory. https://doi.org/10.26023/apfe-d5vh-7d12. Accessed 30 Mar 2019.

Trapp, R. J., Schultz, D. M., Ryzhkov, A. V., & Holle, R. L. (2001). Multiscale structure and evolution of an Oklahoma winter precipitation event. *Monthly Weather Review*, *129*(3), 486–501. https://doi.org/10.1175/1520-0493(2001)129<0486:MSAEOA>2.0.CO;2

Trenberth, K. E., & Fasullo, J. T. (2010). Simulation of present-day and twenty-first-century energy budgets of the southern oceans. *Journal of Climate*, *23*(2), 440–454. https://doi.org/10.1175/2009JCLI3152.1

Twohy, C., Strapp, J., & Wendisch, M. (2003). Performance of a counterflow virtual impactor in the NASA Icing Research Tunnel. *Journal of Atmospheric and Oceanic Technology*, *20*(6), 781–790. https://doi.org/10.1175/1520-0426(2003)020<0781:POACVI>2.0.CO;2

UCAR/NCAR-Earth Observing Laboratory. (2018). NCAR HSRL lidar data. Version 1.0 [Data set]. UCAR/NCAR - Earth Observing Laboratory. https://doi.org/10.5065/d6pk0f1t. Accessed 02 Apr 2019.

Vivekanandan, J., Ellis, S., Tsai, P., Loew, E., Lee, W.-C., Emmett, J., et al. (2015). A wing pod-based millimeter wavelength airborne cloud radar. *Geoscientific Instrumentation, Methods And Data Systems*, *4*(2), 161–176. https://doi.org/10.5194/gi-4-161-2015

Wexler, R. (1955). Radar analysis of precipitation streamers observed 25 February 1954. *Journal of Meteorology*, *12*(4), 391–393. https://doi.org/10.1175/1520-0469(1955)012<0391:RAOPSO>2.0.CO;2

Wexler, R., & Atlas, D. (1959). Precipitation generating cells. *Journal of Meteorology*, *16*(3), 327–332. https://doi.org/10.1175/1520-0469(1959)016<0327:PGC>2.0.CO;2

Wolde, M., & Vali, G. (2002). Cloud structure and crystal growth in nimbostratus. *Atmospheric Research*, *61*(1), 49–74. https://doi.org/10.1016/S0169-8095(01)00102-8

Wu, W., & McFarquhar, G. M. (2016). On the impacts of different definitions of maximum dimension for nonspherical particles recorded by 2D imaging probes. *Journal of Atmospheric and Oceanic Technology*, *33*(5), 1057–1072. https://doi.org/10.1175/JTECH-D-15-0177.1